J. Fluid Mech. (2003), *vol.* 496, *pp.* 1–32. © 2003 Cambridge University Press
DOI: 10.1017/S0022112003005895 Printed in the United Kingdom

Patterns of Faraday waves

By MARK-TIELE WESTRA, DOUG J. BINKS AND WILLEM VAN DE WATER

Physics Department, Eindhoven University of Technology,
PO Box 513, 5600 MB, Eindhoven, The Netherlands

(Received 18 December 2001 and in revised form 18 December 2002)

Faraday waves are standing waves which arise through a parametric instability on the surface of a vertically oscillated fluid layer. They can emerge with various symmetries, simply square to N-fold rotationally symmetric, which for $N > 3$ are quasi-crystalline. In an experiment with a very large aspect ratio we determine the boundaries of the stability regions of waves with different rotational symmetries in the driving frequency–amplitude parameter plane. We find a remarkable agreement with a recent theory by Chen & Viñals (1999) who predict the stability boundaries at the onset amplitude. We argue why such agreement can only be observed in a very large experiment. The main nonlinear damping mechanism of the waves is a three-wave resonance. We devise a simple model that captures this mechanism and that can explain quantitatively the change of the symmetry of the waves with fluid depth. Detailed information about the surface is obtained by scanning the wave field and measuring the phase of subharmonic and harmonic components. Also the results of these measurements compare very favourably to the theoretical predictions.

1. Introduction

In 1831, Michael Faraday published a paper on the behaviour of granular material on a vibrating plate. In the Appendix, he notes that when a fluid is placed on a vibrating plate, it forms ‘crispations’ (waves) which are ‘usually arranged rectangularly with extreme regularity’. He also notes that the frequency of the waves is half the frequency of the vibrating plate.

His findings were confirmed by Lord Rayleigh, who, after papers by Matthiessen (1868, 1870) in which it was stated that the waves oscillated at the same frequency as the plate, performed his own experiments. Rayleigh (1883*a*, *b*) proposed that there might be a connection to the Mathieu equation, which describes parametric resonance. This suspicion was confirmed by the first linear stability analysis of a vertically vibrating inviscid fluid layer by Benjamin & Ursell (1954). They showed that in a non-viscous fluid, the amplitude of an eigenmode of the fluid layer obeys the Mathieu equation.

The Mathieu equation supports solutions at both the frequency of the excitation (harmonic), and at half this frequency (subharmonic). However, in the presence of viscosity, the subharmonic response has smaller dissipation than the harmonic response, and is therefore the one that is excited first.

Experiments performed by Benjamin & Ursell (1954) in a small container (only a few wavelengths across) showed satisfactory agreement with their theory. However, they found that the bulk dissipation could not explain the actual dissipation, which they ascribed to dissipation at the contact line.

A linear stability analysis was performed for viscous fluids of finite depth by Kumar & Tuckerman (1994). Ensuing experiments showed excellent agreement with their theory (Bechhoefer *et al.* 1995; Lioubashevski, Fineberg & Tuckerman 1997). Kumar (1996) points out the possibility of observing the harmonic response at small depth, owing to the large dissipation for long wavelengths in this case. The harmonic response was indeed observed by Müller *et al.* (1997). It was perhaps this effect which was observed by Matthiessen (1868, 1870).

Whilst Faraday observed standing wave patterns in a square arrangement, modern experiments have revealed many other symmetries. If the dissipation is large (a fluid with high viscosity), the preferred pattern consists of parallel stripes (Fauve *et al.* 1992; Edwards & Fauve 1994; Daudet *et al.* 1995). Edwards & Fauve (1994) have also pointed out the importance of the correlation length which determines the influence of the shape of the container on the wave pattern. The square pattern consisting of two perpendicular standing waves which Faraday observed is found at high frequencies (Lang 1962; Ezerskii *et al.* 1986; Tufillaro, Ramshankar & Gollub 1989; Ciliberto, Douady & Fauve 1991; Christiansen, Alstrøm & Levinsen 1992; Müller 1993; Edwards & Fauve 1994). At lower frequencies, a hexagonal pattern consisting of three standing waves spaced at 120° was found by Kumar & Bajaj (1995) and Kudrolli & Gollub (1996). Binks & van de Water (1997) have shown that a whole series of patterns is formed if the container is large enough. Patterns found include square, hexagonal, eightfold and tenfold rotationally symmetric, which consist of $N = 2, 3, 4$ and 5 standing waves, respectively, with wave vectors spaced equidistantly on the circle.

Much of the original experimental and theoretical work done in the 1980s focused on small systems, in which the pattern is determined by the shape of the boundary (Gollub & Meyer 1983; Miles 1984; Ciliberto & Gollub 1985; Meron & Procaccia 1986*a*, *b*; Simonelli & Gollub 1989; Feng & Sethna 1989; Miles & Henderson 1990; Umeki 1991; Gollub 1991; Crawford 1991, 1993). In such systems, only one or a few eigenmodes of the system are excited. The nonlinear dynamics of such systems can often be reduced to a small set of ordinary differential equations which describe the evolution of the amplitude of the eigenmodes. The interaction between modes can give rise to low-dimensional chaotic dynamics, which has been found both experimentally and theoretically (Ciliberto & Gollub 1985). In the 1990s, the interest changed towards large systems, and many experiments were performed addressing questions on pattern selection and chaotic behaviour in large systems (Ezerskii & Rabinovich 1990; Ezerskii 1991; Ciliberto *et al.* 1991; Gollub & Ramshankar 1991; Christiansen *et al.* 1992; Fauve *et al.* 1992; Bosch & van de Water 1993; Gluckman *et al.* 1993; Ezerskii *et al.* 1994).

The amplitude description proved to be a very successful theoretical framework. The assumption is that just above the threshold of the linear instability, the dynamics is dominated by the slow evolution of the amplitudes of the linearly unstable subharmonic modes. For the amplitudes B_n of N interacting standing waves, the amplitude equation reads

$$\frac{\mathrm{d}B_n}{\mathrm{d}t} = sB_n - g_0 B_n^3 - \sum_{\substack{m=1\\ m\neq n}}^{N} g(\Theta_{nm})|B_m|^2 B_n, \tag{1.1}$$

where s is the linear growth rate. The nonlinear saturation of the growth is of cubic order with $g(\Theta)$ the coupling function that gauges the interaction of waves n, m with an angle Θ between the wavevectors. The self-interaction, which involves g_0, is written explicitly. Terms involving a quadratic nonlinearity B^2 are absent as the amplitude equation has to be invariant under the transformation $B \rightarrow -B$. It is dictated by the invariance of the dynamics of the pattern under a shift in time by one period of the excitation, which corresponds to half a period of the linearly unstable waves. This fundamental restraint is lifted when the system is perturbed with a second frequency and transitions between squares, hexagons and triangles can be induced (Müller 1993), however, in the present work we consider monochromatic driving only.

The challenge is to derive the coupling function $g(\Theta)$ from first principles, that is, the Navier–Stokes equation together with the (free-surface) boundary conditions. Once the coupling function is known, the preferred pattern can be obtained simply from (1.1), as we will show later.

The first attempts to derive the coupling function $g(\Theta)$ were reported by Miles (1984), Milner (1991), and Miles (1993) who assumed the fluid to be inviscid, in which case the analysis is greatly simplified. The hope was that viscous effects could be included in a phenomenological way as a perturbation. Milner (1991) obtained an amplitude equation for the inviscid infinite-depth case, valid for purely capillary waves. Although his theory does predict a square pattern above the threshold, the calculation of $g(\Theta)$ contains infinities. It was suggested by Edwards & Fauve (1994) that this is caused by resonant three-wave interactions. In the absence of viscosity, the resonances grow to infinity.

A calculation which includes the effect of viscosity was performed by Zhang (1994) and Zhang & Viñals (1996, 1997*a*, *b*). They use the fact that in the case of an infinite system, viscosity only plays an important role in a thin boundary layer (also called the *vortical layer*) near the free surface, while in the bulk of the fluid the flow is almost completely potential. This leads to the so-called *quasi-potential approximation*, which perturbatively incorporates weak viscous effects by introducing modified boundary conditions at the free surface for the otherwise potential bulk flow. They obtained a standing-wave amplitude equation valid for small viscous dissipation. However, in order to make the problem analytically tractable, they neglected viscous terms with a nonlinear dependence on either the surface displacement, or on the surface velocity. Although the uncontrolled nature of this truncation makes it difficult to assess the region of validity of the theory, their predictions for the stability boundaries of different patterns agree quite well with our experiments (see § 4.3). Depending on parameters, their theory predicts square, hexagonal, eightfold, and patterns of greater rotational symmetry.

Clearly, the prediction of Zhang & Viñals (1996, 1997*a*, *b*) is only valid near threshold and for small viscous dissipation. Hence, when we designed our experiment to test the predictions of their theory, it needed to work with low-viscosity fluids. As will be explained in § 2.4, this necessarily implied that the container size L must be very large. Another reason to consider low-viscosity fluids is that they display much more interesting patterns.

Experiments performed by Kudrolli & Gollub (1996) were in reasonable agreement with the theory by Zhang & Viñals, but the eightfold pattern which was predicted by the theory was not observed. As we will show in § 4.5, the discrepancy is due to the small fluid depth used by Kudrolli & Gollub.

Chen & Viñals (1999) have presented a weakly nonlinear theory of pattern formation which is not restricted to small viscosity. As we will show in § 4.3, the agreement of predictions by this theory with our experimental results is excellent. It is gratifying that the improvement of the theory over that of Zhang & Viñals also leads to an improved agreement with the experiment.

The hydrodynamics of surface waves is complicated by a rotational component of the flow. It was initially believed that the contribution of the corresponding term was $\mathcal{O}(\nu^{3/2})$ in the viscosity, whilst the irrotational part was $\mathcal{O}(\nu)$. This is actually the case in the linear theory. Hence, in the case of the linear stability analysis it is justified to neglect the rotational flow component for small ν. However, for the weakly nonlinear case, Chen & Viñals (1999) show that both contributions to $g(\Theta)$ are of order ν at small ν. Therefore, we cannot obtain the correct form of the amplitude equation if only the irrotational flow is considered.

Faraday surface waves, together with Rayleigh–Benárd convection, is one of the few weakly nonlinear systems for which amplitude equations have been derived from first principles, that is, the Navier–Stokes equations. The availability of a complete weakly non-linear theory for Faraday waves makes the system an ideal test ground for the applicability of the amplitude equation formulation.

In § 2 we will briefly review the amplitude description and illustrate it with plots of the coupling function $g(\Theta)$ for our experimental situation. Next, we explain the three-wave resonance, its intimate connection with the dispersion relation and devise a simple model for $g(\Theta)$ that can explain the dependence of the pattern symmetry on the depth of the fluid layer. We also explain why the experiment has to be so large. In § 3, we describe the experimental techniques used.

So far, most of the measurements conducted in Faraday waves have focused mainly on the stability boundaries of the different patterns. However, the theory also predicts the spatial and temporal phase of the standing-wave field. Whereas a measurement of the stability boundaries of patterns requires only qualitative information on the wave field, for which a shadowgraph method suffices, it is much more challenging to obtain quantitative information about the phases and amplitudes. In § 3.3 we describe a laser refraction technique which provides a precise linear measurement of the surface slope. In fact, because of the accessibility of the free surface, Faraday waves constitute one of the few experiments in pattern formation where the instantaneous hydrodynamic state is accessible.

In order to assess the accuracy of the experiment, we compare in § 4.1 and 4.2 the measured onset amplitudes and dispersion relations with the prediction of linear theory. In § 4.3 we explore the phase diagram of pattern formation of our experiment and compare the phase boundaries with those which are predicted theoretically. The dependence on depth of the surface pattern is studied in § 4.5, it clearly exposes the relevance of the three-wave resonance for nonlinear damping.

Detailed measurements of the amplitudes and phases of the subharmonic and harmonic surface mode components are described in § 4.6. The results are compared with the theory by Chen & Viñals (1999). We conclude that pattern formation of weakly nonlinear Faraday waves is now well understood.

2. The amplitude description

The amplitude equation describes the nonlinear interaction of surface modes that gives rise to patterns. It is instructive to illustrate the amplitude description (1.1) with graphs of the coupling function $g(\Theta)$. As single-wavenumber standing-wave patterns we only consider those where the wave vector directions are equally spaced on the circle. These are also the experimentally observed patterns; they consist of sums of N waves spaced at equal angles $2\pi/N$. Here, $N=1$ corresponds to a pattern of parallel lines, $N=2$ corresponds to two waves at a 90° angle (forming a square pattern), and so on. The question then is which N is preferred at onset.

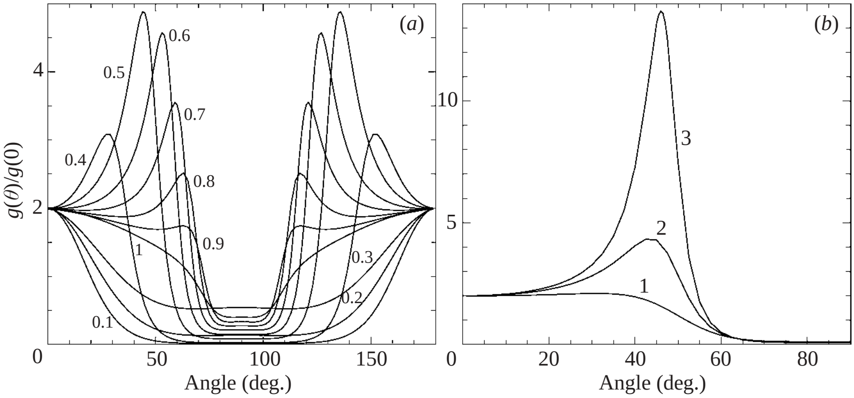

FIGURE 1. (*a*) The coupling function $g(\Theta)/g_0$ at a fixed dissipation $\gamma = 0.037$ and for different values of Σ. The value $\Sigma = 0$ corresponds to a pure gravity wave, $\Sigma = 1$ corresponds to a pure capillary wave. (*b*) Graph of $g(\Theta)/g_0$ for different values of the dimensionless dissipation γ, at $\Sigma = 0.5$. (1): $\gamma = 0.073$, (2): $\gamma = 0.037$, (3): $\gamma = 0.018$.

The computation of the coupling function is a daunting task, and we will show the result by Chen & Viñals (1999). One slight inconvenience is that the coupling function cannot be given in closed form and in order to arrive at results, they have to rely on a symbolic manipulation package to keep track of a very large number of terms that arise when all the terms in the original equations of motion are kept. Nevertheless, several predictions for our experiment were made using software that was kindly supplied by Chen & Viñals.

Before showing the results, we must introduce the dimensionless variables that are pertinent to our problem. The inviscid dispersion relation reads

$$\omega_0^2 = \tanh(k_0 h)\left(g k_0 + \frac{\sigma}{\rho} k_0^3\right), \tag{2.1}$$

where for infinite depth, $\tanh(k_0 h)$ can be set to one. Then, dividing by ω_0^2, we obtain

$$G + \Sigma = 1, \tag{2.2}$$

with $G = g k_0/\omega_0^2$ the contribution from gravity and $\Sigma = \sigma k_0^3/\rho\omega_0^2$ the contribution from capillary forces to the dispersion relation. The case $G = 1$ corresponds to a pure gravity wave, while $\Sigma = 1$ is a pure capillary wave. The fast time and length scales are set by the driving frequency ω_0 and the wavenumber which follows from the inviscid dispersion relation. This readily leads to the dimensionless damping parameter $\gamma = 2\nu k_0^2/\omega_0$.

For N standing waves that are equally spaced on the circle with equal amplitudes, each amplitude obeys

$$\frac{\mathrm{d}B_1}{\mathrm{d}T} = \varepsilon B_1 - g_0 B_1^3 - \sum_{m \neq 1} g(\Theta_{m1}) B_m^2 B_1, \tag{2.3}$$

where ε is the normalized growth rate of the waves, $\varepsilon = s/\gamma\omega$ and Θ_{m1} is the angle between $\boldsymbol{k}_1$ and $\boldsymbol{k}_m$.

To get a feeling for the shape of $g(\Theta)$, we have computed it in several regimes, ranging from the limit of pure gravity waves $\Sigma = 0$, through the mixed gravity–capillary regime, to the limit of pure capillary waves, $\Sigma = 1$. The results are plotted in figure 1(*a*). When Σ is neither close to 0 nor close to 1, so when both surface tension and gravity are important, the coupling function has a resonance peak. As we will discuss in § 2.1, this resonance peak is the result of a three-wave resonance phenomenon. It may already be anticipated that the resonance peaks of the coupling function $g(\Theta)$ play a key role in determining the preferred pattern. As with any resonance, its sharpness is dulled when the viscous dissipation increases, which is illustrated in figure 1(*b*) for several values of the dimensionless damping γ.

The amplitude equation which predicts the preferred pattern can be written in gradient form, with the preferred pattern (that is, the symmetry N) the one that minimizes a Lyapunov functional. Since the form of the Lyapunov functional is an important organizing principle for understanding patterns, we briefly describe it here.

First, note that (2.3) can be written in gradient form as

$$\frac{\mathrm{d}B_n}{\mathrm{d}T} = -\frac{\partial \mathscr{L}}{\partial B_n}, \tag{2.4}$$

in which $\mathscr{L}$ is the Lyapunov function given by

$$\mathscr{L} = -\frac{1}{2} s \sum_n B_n^2 + \frac{1}{4} \sum_m \sum_n g(\Theta_{mn}) B_m^2 B_n^2, \tag{2.5}$$

where $g_0 = g(\Theta_{nn})$ which equals half the value of $g(\Theta \rightarrow 0)$ (otherwise it would be counted twice). From (2.4) and (2.5), it readily follows that $\mathscr{L}$ is a decreasing function of time, therefore, the only possible asymptotic states have stationary amplitudes. Necessarily, those states correspond to minima of the Lyapunov function. Considering only regular patterns with wavenumbers spaced equidistantly on the circle, it is easy to find the N-dependence of the Lyapunov function at stationary amplitude ($\mathrm{d}B_n/\mathrm{d}T = 0$)

$$\mathscr{L}(N) = -\frac{s^2}{4g_0} \frac{N}{1 + \displaystyle\sum_{m=2}^{N} \frac{g(\Theta_{m1})}{g_0}}. \tag{2.6}$$

The minimum argument leaves aside the important question whether the resulting patterns are actually stable with respect to spatial modulations of the amplitude. This question was partially answered by Zhang & Viñals (1998), who show that a numerical integration of the quasi-potential approximation of the Navier–Stokes equation yields patterns that are stable with respect to spatial perturbations.

For our experiment, the computed phase diagram which is spanned by the dimensionless damping γ and the dimensionless capillarity Σ, is shown in figure 2. We see that the regions of preferred patterns show a beautiful nested structure in the (Σ, γ)-plane. For high frequencies, the square ($N = 2$) state is preferred. However, as the excitation frequency is lowered, patterns of higher N come into view. The curves of increasing N converge to the point $\Sigma = 1/3$. This behaviour will be explained in § 2.2.

In the Faraday experiment, we traverse the phase plane by scanning the driving frequency. This corresponds to a trajectory in the (Σ, γ)-plane that is indicated by a dashed line in figure 2. The trajectory is determined by the specific values for the surface tension, density, and viscosity of the fluid that we use, and is such that Σ increases monotonically with increasing driving frequency F.

2.1. *Wave interactions*

The cubic-order nonlinear damping of (2.3) is a three-wave interaction: two subharmonic waves with frequencies ω_1, ω_2 (both equal to $\Omega/2$) couple to produce a third,

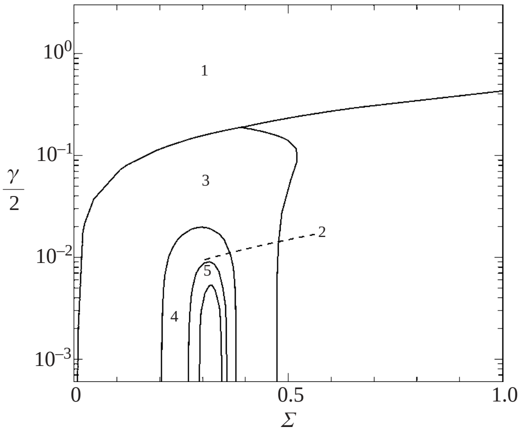

FIGURE 2. Phase diagram of selected pattern as a function of the dimensionless damping γ and the capillary contribution to the dispersion relation Σ. The dashed line is the path that we take through phase space in our experiment when we scan the driving frequency from 25 to 42.5 Hz (see § 4.3). For higher N, the regions converge toward $\Sigma = 1/3$. For smaller dissipation, more of these patterns will be found in the experiment (if it is large enough).

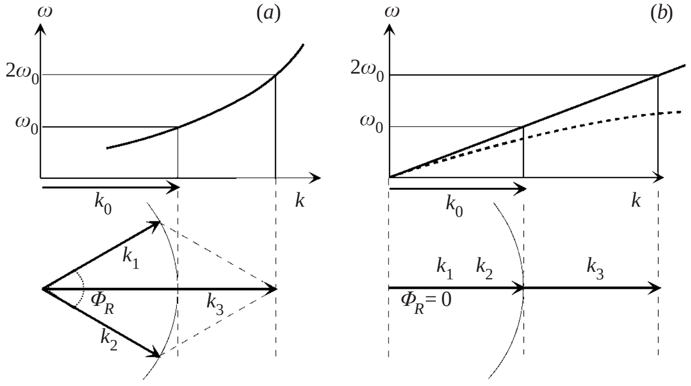

FIGURE 3. The shape of the dispersion relation determines the resonance angle. (*a*) dispersion relation of decay type (see text). In (*b*), the solid line is a dispersion relation that scales as $\omega \propto k$. The dashed line is of non-decay type.

harmonic wave with frequency ω_3. Energy conservation demands that $\omega_1 + \omega_2 = \omega_3$, whereas the wavevectors must satisfy momentum conservation $\boldsymbol{k}_1 + \boldsymbol{k}_2 = \boldsymbol{k}_3$. As the third wave can now couple to the waves with $\omega_{1,2}$ to produce a wave with subharmonic frequency $\Omega/2$, it provides a sink of energy for that wave.

Not only must energy and momentum be conserved for the three interacting waves, but for the energy transfer to be effective, also the dispersion relation must be obeyed, thus

$$\omega(k_1) + \omega(k_2) = \omega(k_3). \tag{2.7}$$

When does resonance occur? The first ingredient is the angle between two linearly unstable modes. The frequency of the nonlinearly generated mode is fixed at $2\omega_0$, but by varying the angle Θ between the primary waves, the wavenumber k_3 can be varied. The second ingredient is the shape of the dispersion relation. Figure 3(*a*) shows how the shape of the (convex) dispersion relation determines the resonance angle Θ_R.

If $\Theta = \Theta_R$, the wave $\boldsymbol{k}_3$ has a wavenumber that satisfies the dispersion relation at frequency $2\omega_0$.

Figure 3(*b*) shows two dispersion relations in which the drawn line scales as $\omega \propto k$, while the concave dashed line scales as $\omega \propto k^p$ with $p < 1$. In the case of the linear scaling $\omega \propto k$, the resonance angle $\Theta = 0$, and the waves $\boldsymbol{k}_1$ and $\boldsymbol{k}_2$ have to be parallel to each other. If the scaling exponent p is smaller than one, meaning that the dispersion relation is concave, the waves $\boldsymbol{k}_1$ and $\boldsymbol{k}_2$ cannot add up any more to the desired wavelength, and three-wave resonance is not possible.

Dispersion relations which scale as $\omega(k) \propto k^p$ with $p > 1$ (convex) are referred to as *decay* type and allow resonant three-wave interactions, whereas if $p < 1$ (concave) the dispersion relation is said to be of *non-decay* type†. For pure gravity waves, the dispersion relation is $\omega = (gk)^{1/2}$, so gravity waves are of non-decay type. However, for pure capillary the dispersion relation is $\omega = (\sigma/\rho)^{1/2} k^{3/2}$, so capillary waves are of decay type. The change of the dispersion relation from non-decay to decay type with increasing frequency (corresponding to a change from concave to convex) has great implications for the pattern formation, as we will see shortly.

The waves with $\omega_0 = \Omega/2$ and k_0 satisfy the inviscid dispersion relation $G + \Sigma = 1$. For other waves, $\omega^* = \omega/\omega_0$, $k^* = k/k_0$, it becomes

$$\omega^{*2} = Gk^* + \Sigma k^{*3}. \tag{2.8}$$

The resonant wave has frequency $\omega^* = 2$, and the resonant wavenumber $k_R^* = |\boldsymbol{k}_m + \boldsymbol{k}_m|/k_0$ obeys $k_R^*(G + \Sigma k_R^{*2}) = 4$. If Θ_R is the resonant angle between $\boldsymbol{k}_m$ and $\boldsymbol{k}_m$, we have $k_R^* = 2^{1/2}(1 + \cos(\Theta_R))^{1/2}$. For the resonance condition, we obtain

$$2^{1/2}(1 + \cos(\Theta_R))^{1/2}[G + 2(1 + \cos\Theta_R)\Sigma] = 4. \tag{2.9}$$

Using $G + \Sigma = 1$, we see that the critical angle Θ_R becomes zero at $\Sigma = 1/3$. Indeed, for $\Sigma < 1/3$, the equation has no solution, so that no resonant angle exists and consequently triad resonance is not possible in the gravity regime.

2.2. *Depth dependence of the resonance angle*

The dispersion relation of Faraday waves is dependent on the depth of the fluid layer. The dependence is strongest for small depths, $k_0 h < 1$. This has a large effect on the resonance angle. The resonance angle as a function of Σ for different depths is plotted in figure 4. The different position of the resonance angle implies a shift of the peak in $g(\Theta)$, and this means that the transitions between patterns will occur at different frequencies.

What is the relevance of wave-interactions for pattern formation? The system chooses the state that minimizes the Lyapunov functional (2.6). The minimum is determined only by the function $g(\Theta)$ and by the number of waves N. From (2.6) we see that for a given N, the absolute value of the Lyapunov function becomes smaller when the sum over the $g(\Theta)$ becomes larger. The value of the Lyapunov function therefore becomes less negative, thereby making the configuration less favourable.

So a $g(\Theta)$ with a peak at Θ_p, say, will tend to disfavour patterns with waves that are separated by the angle Θ_p. Note that the absolute value of the function $g(\Theta)$ is not important, it is the relative difference at different angles that matters. The peak of $g(\Theta)$ changes its position as a function of the excitation frequency, thereby

---

† The name 'decay type' stems from a particle analogy; the wave $\boldsymbol{k}_3$ *decays* in two waves $\boldsymbol{k}_1$ and $\boldsymbol{k}_2$.

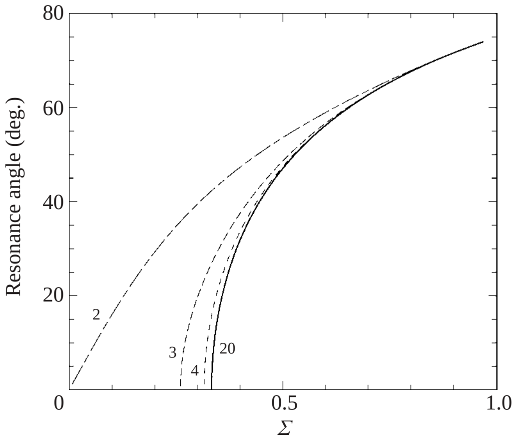

FIGURE 4. Resonance angle Θ_R as a function of Σ for different depths of the fluid. Curves for depths of 2, 3, 4, and 20 mm are shown.

disfavouring different patterns. A change of depth also changes the dispersion relation, and with that the position of the peak in $g(\Theta)$.

The phase diagram of figure 2 is characterized by a nested structure of patterns of increasing rotational symmetry which converges to $N=\infty$ at $\Sigma=1/3$, where the resonance angle becomes zero. This structure can be understood qualitatively by considering the coupling function $g(\Theta)$ in figure 1(*a*). The resonance angle is zero for $\Sigma \leqslant 1/3$, and $g(\Theta)$ becomes concentrated in a resonance peak at small Θ as $\Sigma \downarrow 1/3$. Therefore, the denominator of the Lyapunov function (2.6) can stay small for increasing N if Σ approaches the critical value 1/3.

In conclusion, the overall shape of the coupling function $g(\Theta)$ is determined by resonant three-wave interaction. This elementary process depends on the form of the dispersion relation, which can be tuned by changing the depth of the fluid layer. Below, we will use these ingredients to devise a simple model that captures the dependence of the onset pattern on the depth of the fluid.

2.3. *A toy model*

To illustrate the main mechanism responsible for pattern formation in Faraday waves, we introduce a toy model which highlights the resonance character of three-wave interaction. Three-wave interaction is the result of quadratic nonlinearities. Two waves with amplitude $A_{\boldsymbol{k}_1}$ and $A_{\boldsymbol{k}_2}$ (subsequently called wave 1 and 2) and frequency $\Omega/2$ force a third wave (wave 3) with amplitude $A_{\boldsymbol{k}_3}$. The forced surface mode $\zeta_{\boldsymbol{k}_3}$ satisfies the equation of a driven damped harmonic oscillator:

$$\ddot{\zeta}_{\boldsymbol{k}_3} + \mu(k_3)\dot{\zeta}_{\boldsymbol{k}_3} + \omega_0^2(k_3)\zeta_{\boldsymbol{k}_3} = cA_{\boldsymbol{k}_1}A_{\boldsymbol{k}_2}\cos(\Omega t), \tag{2.10}$$

where $\mu(k_3)$ is the damping of wave 3, $\omega_0(k_3)$ is the frequency of wave 3 according to the dispersion relation and c an irrelevant prefactor. To simplify matters, we take $A_{\boldsymbol{k}_1}=A_{\boldsymbol{k}_2}$ in the forcing term. The amplitude of $\zeta_{\boldsymbol{k}_3}$ is then given by the resonance form

$$A_{\boldsymbol{k}_3} = \frac{cA_{\boldsymbol{k}_1}^2}{\sqrt{(\omega_0(k_3)^2-\Omega^2)^2+\mu(k_3)^2\Omega^2}}. \tag{2.11}$$

We proceed by observing that in the case of dynamical equilibrium, the energy lost by wave 3 comes from waves 1 and 2. We will neglect the possibility that wave 3 spawns

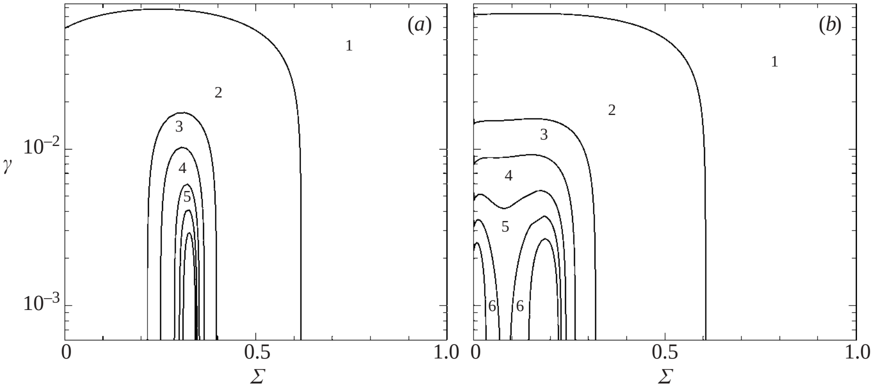

FIGURE 5. Phase diagram of pattern formation computed from the toy model. (*a*) For infinite depth, (*b*) for a depth of 3 mm. The favoured number of waves N is indicated in each region.

waves with yet shorter wavelengths so that its main decay mechanism is through viscous dissipation. Averaged over one cycle of the driving, the viscous energy loss of wave 3 is

$$\tfrac{1}{2}\mu(k_3)\Omega^2 A_{\boldsymbol{k}_3}^2 = \frac{\tfrac{1}{2}c^2\mu(k_3)\Omega^2 A_{\boldsymbol{k}_1}^4}{(\omega(k_3)^2 - \Omega^2)^2 + \mu(k_3)^2\Omega^2}. \tag{2.12}$$

This energy loss is replenished by waves 1 and 2 in the right-hand side of (2.10). For these waves in turn it is an energy loss, so that their energy E_{k_1} diminishes as

$$\frac{\mathrm{d}}{\mathrm{d}t}E_{k_1} = -\tfrac{1}{2}\mu(k_3)\Omega^2 A_{\boldsymbol{k}_3}^2, \tag{2.13}$$

with E_{k_1} the cycle-averaged kinetic energy, $E_{k_1} = \Omega^2 A_{k_1}^2/8$. It then follows that

$$\frac{\mathrm{d}}{\mathrm{d}t}A_{k_1} = -\frac{C\,\mu(k_3)\,A_{k_1}^3}{(\omega(k_3)^2 - \Omega^2)^2 + \mu(k_3)^2\Omega^2} \equiv \beta(\Theta)A_{k_1}^3, \tag{2.14}$$

where we recognize the general form of the amplitude equation (2.3) with the coupling function $\beta(\Theta)$. As we only considered kinetic energy, the factor C is arbitrary, however, its value is irrelevant for our arguments. Of course, the term describing the linear growth of the waves is missing as it was not incorporated in (2.12).

Through a simple energy argument, (2.14) illustrates that the saturation term in the amplitude equation does its work by resonantly coupling waves to waves $\boldsymbol{k}_3$, which are then directly dissipated. Of course, this is an overly simple model and many details are not correct. However, as it embodies the three-wave resonance in a correct way, we expect it to work best for pattern formation where these resonances are crucial.

The function $\beta(\Theta)$ in (2.14) describes the strength of interaction between two waves separated at an angle Θ. In the case of standing waves, we also have the complement angle, so we take our coupling function to be

$$g(\Theta) = \beta(\Theta) + \beta(\pi - \Theta). \tag{2.15}$$

This function can be used in the Lyapunov formalism (2.5) to predict the phase diagram of preferred pattern symmetries N. The result is sketched in figure 5(*a*). It shows the same accumulation of patterns of increasing rotational symmetry around $\Sigma = 1/3$ as the full theory. However, the phase boundaries of $N = 1$ and $N = 2$ states are not predicted correctly. This is not unexpected, as the patterns with low rotational symmetry are also determined by the details of the coupling function far away from the resonant peaks.

The full nonlinear theory by Chen & Viñals (1999) does not incorporate depth, and cannot be easily extended to include it. With our model, we can investigate the influence of depth on the pattern formation. The only change is that we have to use the finite depth dispersion relation in computing the interaction function $g(\Theta)$. The results are shown in figure 5(*b*).

We see that at a fluid depth of 3 mm, the point where the patterns of higher N accumulate shifts to smaller Σ (lower excitation frequency). We also see the appearance of a second series of patterns at very low frequencies. However, it is not clear if this behaviour is to be trusted. It is not easy to check this experimentally, as the frequencies required are very low, so a very large experiment is needed. With our present set-up, this regime cannot be reached.

2.4. *The size of the system*

For interesting physics to happpen, our experiment must be very large. In this section, we consider several aspects of the size of the container. In experiments on Faraday waves, there are three natural sizes which are important. The lateral size of the system L, the wavelength λ, and the *correlation length* ξ, which may be defined as $\xi = 2\pi/\Delta k$. Here, Δk is the band of wavenumbers which are unstable to infinitesimal perturbations.

The correlation length measures the distance over which the pattern is correlated, and therefore measures the size of 'patches' of patterns with possibly different orientations and spatial phases. The *aspect ratio*, which is a measure of the number of different 'patches' is therefore properly defined as L/ξ (and not by L/λ). At $\epsilon = 0$, when the band of unstable wavenumbers has zero width, the correlation length is infinite.

The width of the band of unstable wavenumbers Δk grows as $\Delta k \propto \varepsilon^{1/2}$, and accordingly the correlation length decreases as $\xi \propto \varepsilon^{-1/2}$. Owing to the sidewall boundary condition, the available modes are on a periodic lattice in k-space with mode spacing π/L. The most interesting aspect of pattern formation is its evolution through intrinsic nonlinearities, unrestrained by boundaries. This will occur when the width of the band of unstable wavenumbers becomes equal to the mode spacing Δk, or when the correlation length becomes smaller than the system size L. In this respect, we note that in the small-size experiments mentioned in § 1, the waves are correlated over the entire extent of the system.

In order to find the correlation length, it is necessary to calculate the frequency-dependent prefactor D in $\Delta k = D\varepsilon^{1/2}$, which can be expressed in the curvature of the neutral stability curves of standing waves on a viscous fluid. It was computed using the linear theory of Chen & Viñals (1999) which is elegantly phrased in terms of continued fractions.

In figure 6, we show the ratio of the correlation length and the wavelength λ as a function of ϵ, for different values of the excitation frequency. We can think of ξ/λ as the number of waves in one 'patch'. The solid line in figure 6 corresponds to $\xi = L$, e.g. where the correlation length is equal to the size of the system. The intersection of this line with lines of constant frequency indicates, for a certain ϵ, at which frequency the correlation length is just the container size. For example, the line for an excitation frequency of 20 Hz shows that for $\varepsilon = 0.1$, the correlation length is about 70 times the wavelength. As the wavelength for this frequency is about 2 cm, this means that the

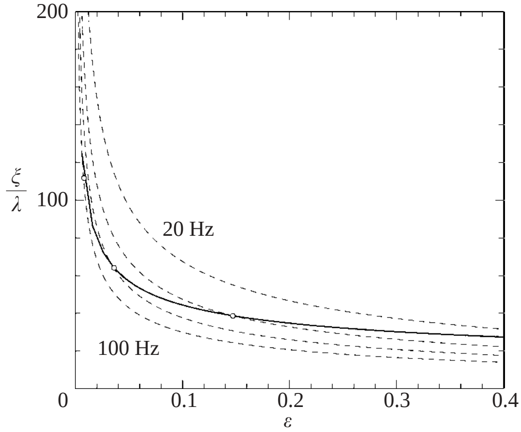

FIGURE 6. The ratio of the correlation length ξ and the wavelength λ for different values of the excitation frequency. The dashed lines correspond (from bottom to top) to 100, 50, 30 and 20 Hz, respectively. The solid line corresponds to $\xi = L$, where L is the size of the system (in our experiment $L = 440$ mm). The intersection of the latter line with the dashed lines (open circles) indicates the ϵ where the correlation length equals the container size.

correlation length is about 1.4 m. Even at $\varepsilon = 0.4$, which is already in the disordered regime, the correlation length is still about 60 cm, which is quite prohibitive for an experiment. On the other hand, at 100 Hz, the correlation length equals our system size (440 mm) already at $\varepsilon = 0.05$. Clearly, the fact that all the interesting pattern formation happens around 30 Hz demands a very large experiment.

Although the system has a continuum of modes available above some ε, the spatial phase that is allowed for the modes is not continuous; the 90° contact angle at the sidewalls provides a 'phase rigidity' there. As a consequence, the position of the sidewalls is felt in a large region of the container, even though the modes may be continuous. This may lead to non-trivial time averages of the chaotic surface (Gluckman *et al.* 1993, 1995; Ning *et al.* 1993; Bosch, Lambermont & van de Water 1994; Eguíluz *et al.* 1999), even for ε way into the disordered regime.

3. Experimental

An accurate check of the validity of the weakly nonlinear theory of pattern formation puts stern demands on the design of the experiment. First of all, the theory is 'weakly nonlinear', meaning that it is valid only just above the threshold of the linear instability. We therefore need very good control over the dimensionless distance from threshold ε. Both spatial variation of ε over the container, and slow variation of ε in time have to be avoided with great care. That the long-time stability of the experiment is important stems from the fact that at small ε the dynamics experiences a 'critical slowing-down', meaning that the slow time scale diverges. In order to obtain a defect-free pattern, for example, we often have to wait several hours.

A second problem is that the size of the system is finite, whereas the theory was formulated for the infinite system. Matters of size have been discussed in the previous section, with the unavoidable consequence that the physical size must be large indeed. To our knowledge, our experiment is the largest experiment on Faraday waves conducted so far.

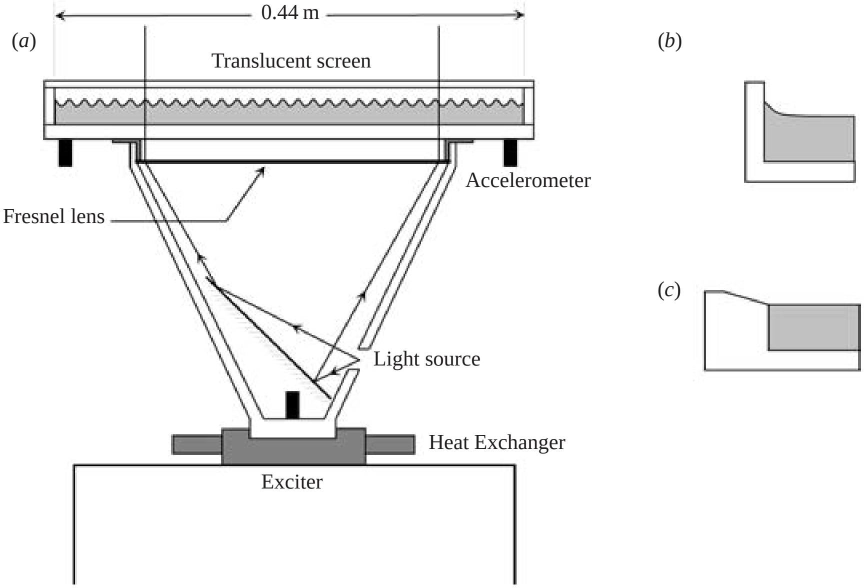

FIGURE 7. (*a*) Schematic overview of the container and support structure. (*b*) Vertical wall boundary condition, (*c*) sloping wall boundary condition.

3.1. *Shape and size of the container*

The shape and size of the container have many effects on the experiments. As the theory described in § 2 is valid only for systems infinite in the lateral extent, the most important concern is the size of the experiment and the corresponding mode quantization. As explained in § 2.4, the width of the band of unstable wavenumbers increases with the excitation strength ε. As argued in that section, we expect the system to become insensitive to the size of the system above a certain ε, where the unstable wavenumbers form a continuous band. The smaller the size of the system, the higher the required ε. For a comparison with theory, which is valid only at threshold, this means that the system size should be as large as possible.

A schematic overview of the experimental set-up is shown in figure 7(*a*). We use a circular container with a diameter of 440 mm and a vertical wall boundary. The bottom of the container is a 15 mm thick glass plate, the wall consists of a Perspex ring of 25 mm height. At this size, the expected mode continuum occurs below $\varepsilon \approx 0.1$ for excitation frequencies between $F = 25 \ldots 40$ Hz.

The shape of the edge determines the boundary condition. The boundary of figure 7(*c*) allows the container to be filled to the rim, with the sloping sidewall (whose slope equals the contact angle) just wetted by the spilling fluid. This 'brimful' condition is the best approximation of a pinned boundary. Because of the low surface tension of the fluid used in our experiment, the sidewall of the container is always covered with a very thin layer of fluid. For making a pinned boundary condition, we have to let the fluid settle for a long time. However, all but the smallest wave amplitudes cause the fluid to wet the edge in a manner dependent on the mode present. Moreover, very slight differences in the height of the fluid result in large changes of the boundary condition.

Because of the difficulty in realizing a pinned boundary condition, we decided only to use a vertical wall boundary condition in the large circular container (figure 7*a*).

Another effect of the pinned boundary condition is the strong quantization of modes. In the case of the vertical wall boundary condition, the wetted sidewall provides a ‘soft’ mode quantization, which in effect makes good patterns possible before we would expect them on the basis of the continuum argument sketched in § 2.4.

In a circular container, the orientation of the wave patterns is undetermined and is found to drift slowly in time. In some of our experiments, we are interested in the temporal and spatial phase of the surface waves. Our experimental technique to measure those needed a pinned surface. This was done in a square container with sidewalls of 160 mm length and a sloping edge of 20 mm height, as shown in figure 7(*c*). For ease of construction, the square container is simply placed inside the large circular container.

Straight sidewalls emit a meniscus wave. This is because the length of the meniscus (which is set by $l=(\sigma/(g\rho))^{1/2}$) depends on the acceleration due to gravity. When the cell goes up, the effective gravity increases and the meniscus length decreases. In order to preserve mass, a surface wave is emitted. As the wave is directly forced, it has the same frequency as the drive, and it is always present.

As stated before, the meniscus wave can be overcome by using the ‘pinned’ boundary condition. In practice, our container is large enough for the meniscus wave to be damped out in the measurement region. The decay length of the meniscus wave can be estimated by $l_{\text{decay}} \approx (\omega/2k)/(2\nu k)$, which is just the velocity of the meniscus wave multiplied by the viscous decay time. In our case, $l_{\text{decay}} \approx 40$ mm for $F = 30$ Hz. As our container has $\varnothing = 440$ mm, the meniscus wave is easily avoided.

Levelling is done using the experiment itself: just above threshold we immediately notice small level faults as an inhomogeneity of the surface pattern. The levelling error was measured with a sensitive water level and, at the sidewalls, the deviation of the mean depth was found to be ≈ 0.1 mm in the case of the circular container ($\varnothing = 440$ mm), and ≈ 0.03 mm for the square container (160 mm square). The depth of the fluid, which varies from 2 to 20 mm, is determined by measuring the volume of the fluid. As we have a large container ($\varnothing = 440$ mm) an error of 1 ml in the volume gives rise to an negligible error of ≈ 7 μm in the depth. Therefore, the largest error in the depth is due to the levelling error. If not specified otherwise, a fluid depth of 20 mm was used which can be considered as infinitely deep, as will be argued in § 4.5.

3.2. *Excitation, fluid and temperature control*

The large circular container is attached to a hollow aluminium conical structure (see figure 7). The cone is attached at approximately 2/3 the radius of the container to suppress the lowest mechanical vibration mode of the bottom plate of the container. Inside the cone, several devices can be placed, i.e. mirrors or detectors. The entire structure is mounted on top of a Ling Dynamic Systems electromagnetic exciter that can deliver a maximum force of 2900 N.

The exciter is driven using a computer controllable NF Electronic Instruments 1930A frequency synthesizer. The frequency is constant to 1 part in 10^6. The signal is amplified with a Ling Dynamic Systems power amplifier, with a maximum power of 2000 W. The acceleration amplitude is measured by means of piezoelectric accelerometers with one high-resolution sensor mounted to the bottom centre of the cone, and two lightweight sensors which may be mounted at various positions on the container.

The amplitude of the acceleration is determined using a discrete Fourier transform on an integer number of periods of the drive. Mainly because of temperature effects, the ratio between the output signal of the power amplifier and the actual amplitude of the exciter is not a constant. Therefore, we use a simple linear control loop to keep the actual acceleration amplitude constant. In this way, the amplitude is constant to within 0.3 %.

The quality of the acceleration was checked by measuring the signal of the high-resolution accelerometer at the bottom of the cone at a frequency of 30 Hz and an amplitude of 0.28 g. The power spectrum of this signal showed no discernible higher harmonics of the 30 Hz signal.

As most of the interesting pattern formation takes place between 25 and 40 Hz, we have constructed both the container and the supporting cone to have their resonances at high frequencies. The lowest resonant mode of joint vibration of container and cone lies at ≈ 590 Hz. Although the materials used have low internal damping, some of the found structural resonances were appreciably broadened. In order to minimize their influence at the frequencies of interest, it was important to move them to high frequencies by structural adaptations.

The exciter itself has two resonances, which both correspond to side-to-side motion. The first occurs at 20 Hz, the second at 40 Hz. At the frequency range of interest (25–40 Hz), the major contribution to inhomogeneity of the acceleration is due to these modes. To gain insight into the inhomogeneities of acceleration, we simultaneously measured the acceleration at the bottom of the cone and at four positions on the edge of the container using two accelerometers. By careful mechanical tuning, it was possible to move all resonances out of our frequency window of interest such that in the region of interest (25–35 Hz), the acceleration inhomogeneity is smaller than 2%.

The fluid we use is a low-viscosity low-surface-tension silicon oil (Tegiloxan 3 produced by Goldschmidt AG, Essen, Germany). At 21 °C, its specified surface tension is $\alpha = 18.3 \times 10^{-3}\,\mathrm{J\,m^{-2}}$, which is within 0.5% of the measured value. The measured viscosity is $\nu = (3.63 \pm 0.03) \times 10^{-6}\,\mathrm{m\,s^{-2}}$, and specified density $\rho = 892.4\,\mathrm{kg\,m^{-3}}$. The tendencies of the fluid parameters with temperature are such that they are constant to within 0.1%, given our temperature control.

Owing to the low surface tension, the oil forms a thin smooth layer on the vertical walls and on the covering glass plate, which greatly facilitates optical accessibility. If we use water, for example, droplets quickly form on the covering glass. The wetted sidewalls guarantee a ‘soft’ boundary condition.

Another advantage of the low surface tension is that no surface film is formed on the free surface of the fluid. If we use water, after a short period of time, a surface film is formed which completely changes the surface tension. As shown by Henderson & Miles (1994), the presence of a surface film can strongly affect both the surface tension and the damping at the free surface. The finite compressibility increases the dissipation of energy in the boundary layer. This problem has been studied thoroughly by Miles & Henderson (1998). Owing to the relatively short molecular chains, the low-viscosity silicon oil we use behaves like a Newtonian fluid. Only the higher-viscosity silicon oils show non-Newtonian behaviour.

The temperature of the whole construction is kept constant to within 0.03 °C. To this end, the whole construction is placed in a temperature controlled room with temperature 21.0 ± 0.1 °C. The construction is insulated from the (heat producing) exciter with a water-cooled heat exchanger. The cooling water is kept at 21.0 ± 0.1 °C. Measured temperature fluctuations inside the container are down to 0.03 °C.

The light source used in the shadowgraph technique (see § 3.3) is a standard 150 W incandescent halogen lamp which illuminates a multi-stranded optical fibre after passing through a heat filter. As no significant temperature change is observed after

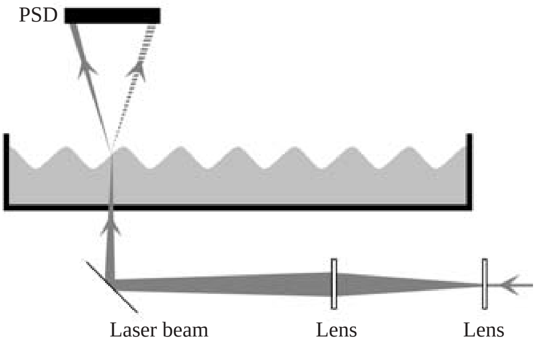

FIGURE 8. Principle of the laser refraction method.

turning on the lamp, it may be concluded that the use of the heat filter is sufficient, and that absorption of light in the fluid may be neglected.

3.3. *Measuring waves*

To visualize Faraday waves, the shadowgraph technique is often used. It visualizes the free surface using the refraction of parallel light incident from below. A Fresnel lens (see figure 7) is used to render the light parallel. The waves focus or defocus the light, which then forms bright and dark spots on a screen placed above the container.

Images of the surface are made using a 1024 × 1024 8-bit CCD camera with a liquid crystal shutter. A programmable hardware system allows us to control the phase at which the image is taken. The integration time of the image is kept well below half the period of the wave, so that the image can be considered as an instantaneous snapshot of the surface. The images are processed and stored in a dedicated digital imaging system. The fundamental nonlinear nature of the imaging process, however, restricts the method to obtaining only qualitative information of the wave field.

A precise linear measurement of the elevation $\zeta(x, y)$ over the entire surface is difficult. A noteworthy attempt to use diffusing light scattering was reported by Wright, Budakian & Putterman (1996). In our experiment, we use a laser refraction method which gives an accurate linear measurement of the surface slope in a point. The principle is sketched in figure 8.

A laser beam is focused onto the surface and the position of the refracted beam is measured with the help of a position sensitive device (PSD) with a surface area of $20 \times 20\,\text{mm}^2$. The x and y position signals of the PSD sensor are low-pass filtered at 10 kHz and sampled with a 12-bit ADC at 20 kHz. From the position of the light spot on the PSD and the distance of the PSD to the fluid surface, the surface slope $(\partial\zeta/\partial x, \partial\zeta/\partial y)$ follows from an elementary geometrical argument. The linearity of the slope measurement is better than 0.1%.

Owing to the long time scales involved in Faraday waves, the experimental set-up is completely automated. This automation allowed us to perform careful experiments that human impatience would otherwise prevent.

4. Experimental results

4.1. *Linear behaviour: onset*

The onset driving amplitude and the dispersion relation for Faraday waves is predicted by well-established linear theory (Kumar & Tuckerman 1994). Still, we find it useful to compare these predictions to experiments, as it provides a check on the accuracy

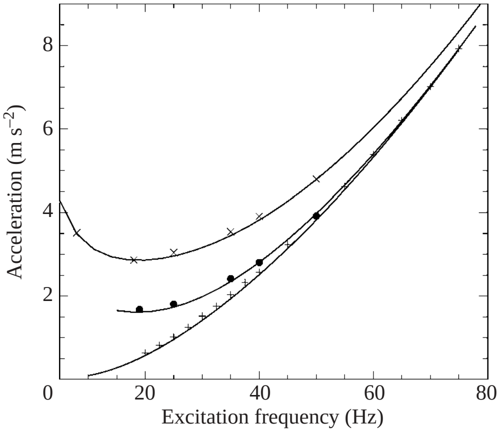

FIGURE 9. Onset of the linear instability as a function of frequency. +, depth of 25 mm; ●, 3 mm; ×, 2 mm. Full lines: theoretical predictions.

of both experiment and theory. The onset driving amplitude is determined by the effects of bulk viscosity and bottom friction.

To measure the onset of the linear instability, the control parameter is slowly increased, and the presence of subharmonic waves is assessed by eye. The results for the onset for various depths of the fluid layer are shown in figure 9. As was also found by Bechhoefer *et al.* (1995), Kumar (1996) and Lioubashevski *et al.* (1997), the experiment agrees well with the predictions from linear theory. The theoretical onset curves were computed using a viscosity $\nu = 3.67 \times 10^{-6}\,\mathrm{m}^2\,\mathrm{s}^{-1}$, which is not significantly different from the measured value. In fact, the precision of experiment and theory makes linear Faraday waves a system that can be used to measure both surface tension and viscosity. In very small containers, sidewall friction is known to affect the onset acceleration. For the large container (440 mm diameter), we expect this effect to be negligible.

4.2. *Linear behaviour: the dispersion relation*

In § 2.1, it was emphasized that pattern formation depends crucially on the precise shape of the dispersion relation. Therefore, it is important to measure the dispersion relation in the experiment and compare it to the theoretical prediction. In our measurement we make use of the fact that at a given frequency ω_0, the fastest growing wave has wavenumber k_0. If we change the excitation abruptly from a value beneath onset to a value about 20% above onset ($\varepsilon = 0.2$) we observe the formation of a concentric set of circular waves (see figure 10*b*). This circular pattern (which is not a Bessel pattern) soon breaks up. However, we can capture the first pattern by the digital camera if we time it correctly. The maxima of figure 10(*b*) are spaced equidistantly and the wavelength is the mean spacing. Of course, just above threshold, we do observe Bessel modes. The circle-symmetric pattern shown in figure 10(*b*) is already far above threshold, so many Bessel modes are excited. The observed pattern is therefore not a fundamental mode of the system, but consists of many of them.

The experimental results for depths of 2 and 20 mm are shown in figure 10(*a*), together with the theoretical predictions of the inviscid finite depth linear theory and the viscous theory by Kumar & Tuckerman (1994). We see that at a depth of 20 mm, the inviscid theory already gives a good approximation of the dispersion relation; the

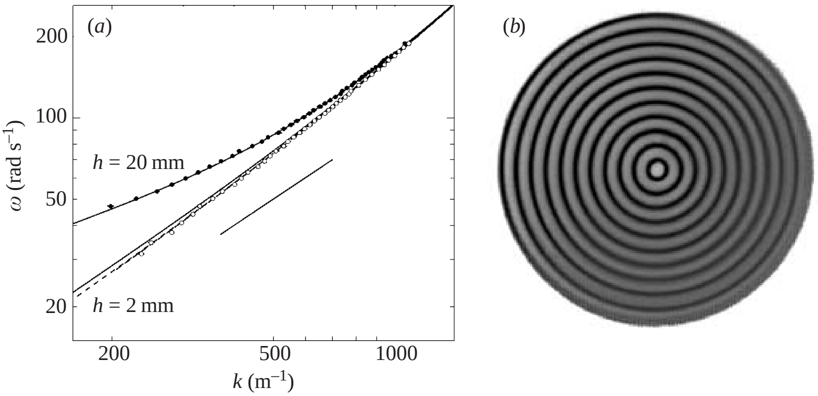

FIGURE 10. (*a*) Dispersion relation $\omega(k)$ plotted on a log–log scale. The angular frequency ω of the waves is equal to half the excitation frequency. ●, experimental data for a depth of $h = 20$ mm (effectively infinite for this range of k). ○, measurements for a depth of $h = 2$ mm. —, $\omega^2(k) = \tanh(kh)(gk + (\sigma/\rho)k^3$ for $h = 20$ and $h = 2$ mm (lower line). – – –, viscous theory Kumar & Tuckerman (1994) for $h = 20$ mm (the line corresponding to $h = 20$ mm is not visible as it coincides with the solid line) and 2 mm (lower line). The short line segment designates the linear dependence $\omega \propto k$. (*b*) Pattern observed just after the excitation amplitude is changed abruptly from zero to $\varepsilon \approx 0.2$ at an excitation frequency of 25 Hz. Owing to restrictions in the visualization, only the central 2/3 fraction of the container is shown.

effect of viscosity can only be felt at very shallow depths. The experimental results agree perfectly with theory.

4.3. *The phase diagram of pattern formation*

The theoretical phase diagram shown in figure 2 predicts the existence of nested regions in parameter space with patterns of increasing rotational symmetry. In the experiment, we indeed find many patterns with different rotational symmetries, as shown in figure 11.

Note that the patterns with 4- and 5-fold rotational symmetry in figures 11(*c*) and 11(*d*) are special: they do not fill the plane regularly. For this reason, they are often called *quasi-crystalline patterns*. It is well known that only patterns with 2- and 3-fold rotational symmetry (e.g. squares and hexagons) can fill the plane regularly, and it was long believed that patterns with 5-fold symmetry did not exist in nature.

It is a challenge to verify the whole phase diagram of pattern formation in the experiment. Because near phase boundaries the dynamics slows down critically, we have devised automated procedures to detect the presence of patterns with a given symmetry.

In order to determine the phase diagram, we scan (ε, F)-space, where F is the excitation frequency and ε the dimensionless distance from threshold. At each value of F, we determine the pattern at different values ε above threshold. The boundaries in the phase diagram were determined in two ways. The first consists of quasi-static upward scans in ε at a fixed frequency. The slow dynamics of the system dictate long measurement times. The amplitude is increased in steps of $\approx 1\%$, then held for 2000 s after which 5 images with 1000 s intervals are taken to observe any temporal dependence. As a check that we do not introduce any hysteresis in this manner, we perform a second scan, this time with fixed ε and increasing frequency F. At each value of ε and F, we started with zero excitation amplitude ($\varepsilon = -1$), and then jumped to the desired value. In this way, any artificial introduction of hysteresis in

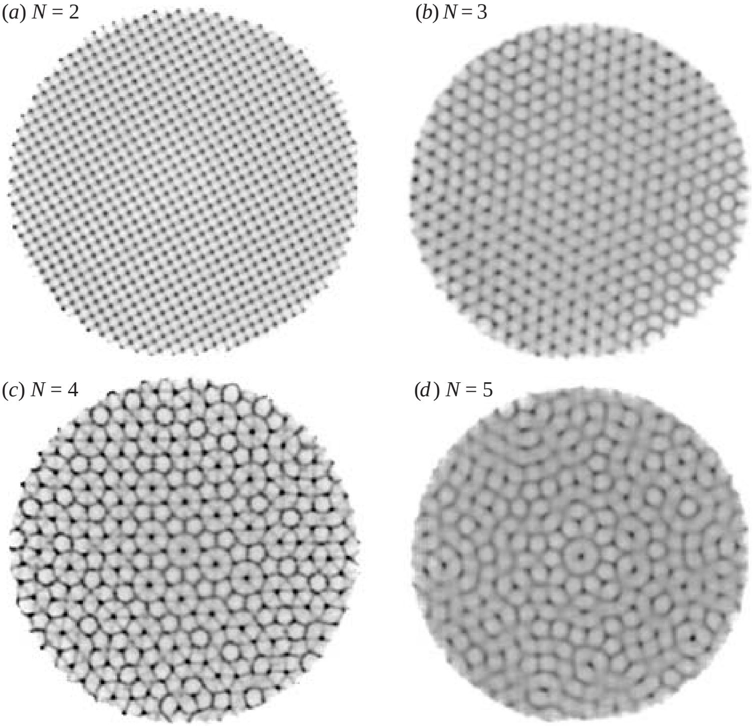

FIGURE 11. Shadowgraph images of the fluid surface at (*a*) $F = 45$ Hz, (*b*) $F = 30$ Hz, (*c*) $F = 29$ Hz, (*d*) $F = 27$ Hz. $\varepsilon = 0.1$ in all cases. The patterns correspond to $N = 2, 3, 4$ and 5 standing waves, respectively. Again, only the centre 2/3 part of the container is visualized. The appearance of both hexagons as triangles in (*b*) is explained in § 4.4.

the patterns was prevented. There were no observed differences in the results of both methods.

Just above onset, only few modes are exited. In the circular container this gives rise to Bessel modes. At higher ε, enough modes are excited to form regular patterns. As discussed in § 2.4, we expect Bessel modes below the line $\Delta k = \pi/L$, and regular patterns above this line.

In order to automatically recognize the pattern, we first compute the two-dimensional power spectrum of the image, which is obtained from the two-dimensional Fourier transform in the usual way. We then perform an angular correlation in the power spectrum, which effectively determines how many angular maxima the spectrum has. An n-fold symmetric pattern will have $2n$ peaks in its power spectrum on a circle of radius k. In order to bring out the regular spacing of the peaks more clearly, we compute from each power spectrum ($P(k, \theta)$), the angular correlation function $C(\phi)$ averaged over a band of wavenumbers of width $\approx k$.

$$C(\phi) = \left\langle \frac{\Sigma_\theta [P(k, \theta) - \bar{P}][P(k, \theta - \phi) - \bar{P}]}{\Sigma_\theta [P(k, \theta) - \bar{P}]^2} \right\rangle . \tag{4.1}$$

In comparison with other methods (Kudrolli & Gollub 1996), the resulting function $C(\phi)$, will for an n-fold pattern have peaks at precisely $2\pi/n$, independent of the orientation of the pattern and the k range over which $C(\phi)$ is averaged. This last point is crucial, as higher spatial harmonics can lead to extra peaks in $C(\phi)$ if $P(k, \theta)$

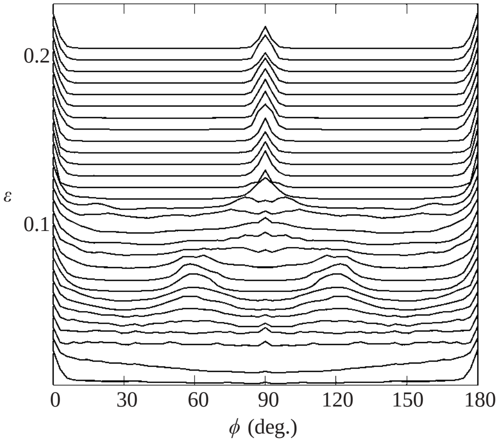

FIGURE 12. Graph of the angular correlation $C(\phi)$. A slow upward scan in ε was performed at $F = 35$ Hz. The range extends from $\varepsilon = 0.01$ to $\varepsilon = 0.23$. Each line is an average over 5 images taken 200 s apart.

is summed over k before computing $C(\phi)$. These higher harmonics unavoidably arise owing to imaging nonlinearities.

As an example, we show in figure 12 the function $C(\phi)$ for the states that are encountered in a slow upward scan of ε at $F = 35$ Hz. For each ε, $C(\phi)$ was averaged over five images taken 200 s apart. Figure 12 shows the transition from the flat state below onset to the hexagonal state with peaks at 60° and 120°, which in turn gives way to the square state with a peak at 90°.

In figure 13(a) we show the phase diagram of Faraday waves obtained by the methods explained above. Just above onset, we see Bessel modes. At higher ε, regular patterns set in. We see a cascade of patterns with changing frequency, going from squares at high frequency through hexagons to 4-fold, and eventually 5-fold rotationally symmetric patterns. The square and hexagonal patterns coexist in a large transition region. Although there is probably also a transition region between the $N = 3$ and $N = 4$ regions, it is too narrow to be determined in this experiment.

Exactly at onset, the correlation length $\xi = 2\pi/\Delta k$ diverges, and the boundary conditions discussed in the previous paragraphs are felt. The large circular container has a diameter of 440 mm. As shown in § 2.4, the continuum is reached at $\varepsilon = 0.04$ at 30 Hz. In the phase diagram figure 13, we clearly see that patterns emerge at reduced driving amplitudes above the line $\Delta k = \pi/L$. However, the best patterns are seen around $\varepsilon = 0.1$. At very low fequencies, we observe Bessel modes well above the line $\Delta k = \pi/L$. Strictly speaking, at $F = 25$ Hz the *correlation length* equals the size of the container (corresponding to $\Delta k = 2\pi/L$) at $\varepsilon \approx 0.32$. Clearly, the mode spacing argument is crude, and does not allow for the mode structure of the circular container and the details of the boundary condition at the vertical walls. To stress once more the importance of size, we note that had we used a container of diameter 100 mm, the continuum at 30 Hz would lie at $\varepsilon = 0.59$, which is well into the disordered regime.

The lines in figure 13(b) denote the phase boundaries of different patterns. The transition frequencies at threshold were determined by the points were the lines cross the $\varepsilon = 0$ line. Using the parameters of our fluid, and using the program which was kindly provided to us by Chen & Viñals, we computed the theoretical results for the transition frequencies. They are compared to the experiment in table 1. The frequencies

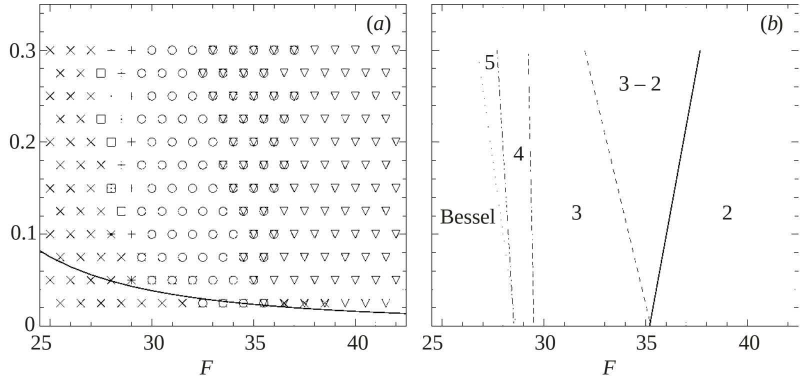

FIGURE 13. (*a*) Phase diagram of pattern formation. $\triangledown$, $N = 2$; $\circ$, $N = 3$; $+$, $N = 4$; $\square$, $N = 5$; $\times$, Bessel modes. The solid line corresponds to the line where $\Delta k = \pi/L$. (*b*) Lines drawn through transition regions. The solid line and the right-most dashed line delimit the transition region from an $N = 2$ to an $N = 3$ pattern. In the region marked $3 - 2$, both square and hexagonal patterns coexist. The dashed line in the middle is the boundary between the $N = 3$ and the $N = 4$ regions. The dot-dashed line is the boundary between the $N = 4$ and $N = 5$ regions. The dotted line is the boundary between the $N = 5$ and the Bessel mode region.

Transition	Experiment	Theory
$2 \rightarrow 3$	35.3 ± 0.3	35.4
$3 \rightarrow 4$	29.5 ± 0.9	28.4
$4 \rightarrow 5$	28.6	none

TABLE 1. Transition frequencies.

of the first two transitions are seen to agree with theory, approximately to within the experimental uncertainty. Considering that the theory contains no fitted parameters, this is remarkable. According to the theory, the experimental trajectory through the (Σ, γ)-phase plane of figure 2 would just miss the region in which the 5-fold rotationally symmetric pattern is preferred; still, we do observe it around $F = 28$ Hz. Both the observed $N = 5$ pattern and the value of the predicted $3 \rightarrow 4$ transition, point to a slight discrepancy with theory. On the other hand, the corresponding frequencies are so low that we may start to feel the finite size of the experiment.

4.4. *Triangles versus hexagons*

Looking at the $N = 3$ patterns of figure 11(*b*), we note that some parts of the figure appear as hexagons and other parts as triangles. This is caused by the fact that if we add three standing waves at equal angles, we have the freedom to choose the spatial phase of one of the waves. Figure 14 shows the effect of shifting the spatial phase of one of the waves over $\pi/2$ radians. Clearly, whether the surface appears as hexagons or triangles depends on the spatial and temporal phases of the waves.

The spatial phase of the waves is undetermined at the order of the nonlinearity of the theory described here. In other pattern forming systems showing a pattern with three waves at a mutual angle of 120°, or in the case of two-frequency forcing of Faraday waves, the spatial phase is determined by quadratic terms in the amplitude equation (Edwards & Fauve 1994), whilst quintic terms were considered by Müller (1993). These quadratic and quintic terms then determine whether the system forms

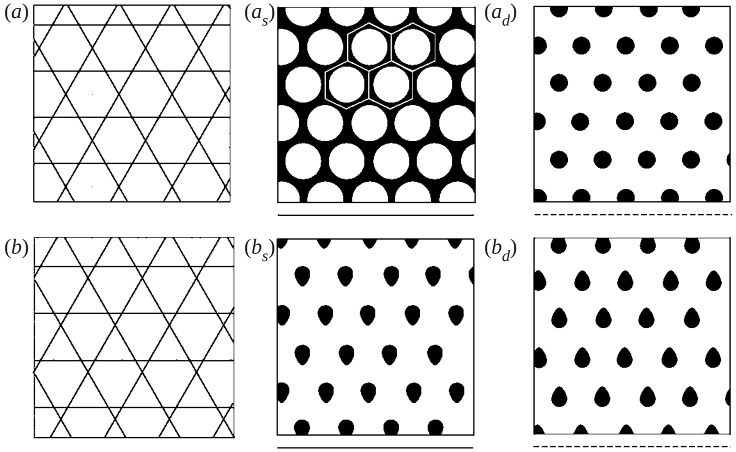

FIGURE 14. The effect of the spatial phase. (a) and (b): patterns consisting of three standing waves at a 120° angle. The solid lines denote the maxima of the waves at time zero, the dashed lines show the maxima half a period of the wave later. In (b), the position of the horizontal wave has been shifted downwards by $\pi/2$. (a_s) and (b_s): wave heights corresponding to the solid lines in (a) and (b), respectively (black regions correspond to high surface elevation). (a_d) and (b_d): wave heights corresponding to the dashed lines in (a) and (b), respectively.

hexagons or triangles, and usually no mixed region is seen in these cases. As explained in § 1, we do not have quadratic terms in the amplitude equation describing Faraday waves due to the subharmonic symmetry $A \rightarrow -A$, and close to threshold, quintic contributions are very small.

4.5. *Effects of fluid depth on patterns*

The change of the pattern symmetry with fluid depth is a profound consequence of the three-wave resonance which strongly organizes the nonlinear damping of Faraday waves. In § 2.1, we discussed the influence of the dispersion relation on pattern formation. From the inviscid expression (2.1) it is seen that the shape of the dispersion relation can be changed by altering the depth, with the relevant factor $\tanh(kh)$. Correspondingly, the depth (z) dependence of the velocity field is for deep fluids given by e^{kz}. Comparing the value of e^{kz} (for 25 Hz, where $k \approx 445\,\mathrm{m}^{-1}$) at $z = -2$ mm and $z = -20$ mm, (0.41 and 0.0001, respectively), we see that even at a depth of 20 mm, the velocity is already very small compared to the velocity at the surface. We therefore expect that, given the range of frequencies we use in the experiment (25–45 Hz), even moderate depths ($\approx$ 20 mm) can effectively be considered infinite, as there will be only a very small effect on the flow. This expectation is clearly corroborated by figure 10, where the experimental dispersion relation for a depth of 20 mm coincides with the analytical infinite depth dispersion relation. As long as the dimensionless ratio between wavenumber and depth kh is large, the system can be considered infinitely deep. This means that for lower frequencies (with smaller wavenumbers), the approximation becomes worse.

The dramatic influence of finite fluid depth on the symmetry of the threshold pattern is illustrated in figure 15, where we observe at the same excitation frequency and amplitude a four-fold rotationally symmetric pattern at depth $h = 10$ mm and a hexagonal pattern at $h = 3.5$ mm. The complete phase diagram is shown in figure 16. We see that for smaller depth, both transition frequencies shift to lower values.

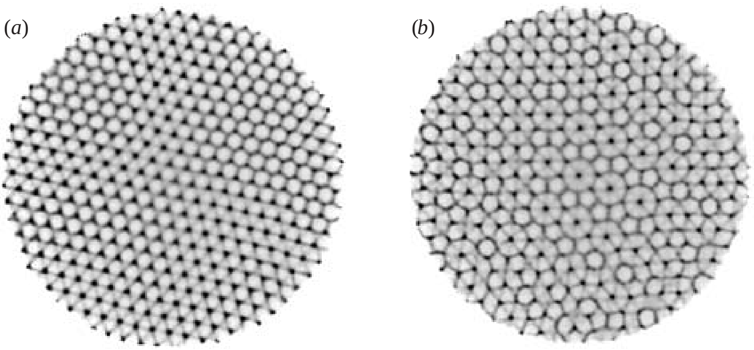

FIGURE 15. Shadowgraph images of the fluid surface at $F = 29\,\text{Hz}$ at $\varepsilon = 0.1$. (*a*) Depth of 3.5 mm showing a hexagonal pattern, (*b*) depth of 10 mm showing a pattern consisting of four standing waves.

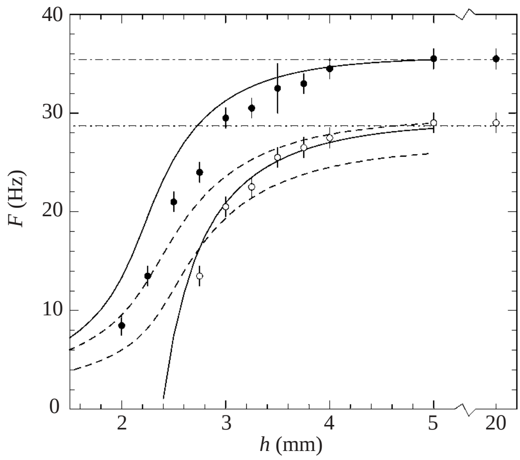

FIGURE 16. Boundaries between different pattern symmetries at $\varepsilon = 0.1$ in the driving frequency-depth plane. ○, 3–4 boundary. ●, 2–3 boundary. The error bars denote the width of the transition region from one pattern to another. –·–, predictions from Chen & Viñals (1999) for infinite depth. – – –, transition computed from the toy model in § 2.3. —, contours of constant resonance angle (using the viscous dispersion relation) chosen so that at infinite depth they pass through the transition frequencies.

The form of this phase diagram can be understood very well from the change of the dispersion relation with depth. As explained in § 2.1, pattern formation at these frequencies is strongly influenced by a three-wave resonance which is characterized by a resonance angle Θ_R between the wavevectors. The resonance angle changes with depth in a characteristic way such that Θ_R decreases when the depth decreases (see figure 4). It is precisely this change that causes the transition of one type of pattern formation to another. The solid lines in figure 16 are lines of constant resonance angle $\widetilde{\Theta}_R$ which were forced to pass through the phase boundaries at infinite depth by the appropriate choice of $\widetilde{\Theta}_R$. They trace the observed phase boundaries rather well, which demonstrates that the change of we pattern symmetry to another is set by a three-wave interaction at a particular value of the resonance angle.

Whilst lines of constant resonance angle are a relative prediction, the absolute phase boundaries can also be computed using the model of § 2.3. These predictions are shown as the dashed lines in figure 16. Because our model does not reproduce well the coupling function away from the resonant peaks, the absolute prediction of the depth-dependent boundaries has a much larger error.

4.6. *Measurements of the wave field*

Nonlinear damping through wave coupling implies that many waves are present on the surface, each with its own frequency and (temporal) phase. The weakly nonlinear theory by Chen & Viñals (1999) predicts the properties of these waves, at least up to order ε, i.e. the waves with harmonic frequency Ω. A measurement of the associated amplitudes and phases requires an extremely linear measurement of the surface. Using the laser refraction method of § 3.3, we are able to measure the surface slope in a single point. In this section, we explain that such a measurement yields amplitudes and phases of various waves which can be compared to a theoretical prediction.

Our emphasis will be on a measurement of the detailed surface structure, not on absolute values of amplitudes. The absolute amplitude of the subharmonic wave in a striped pattern was measured by Wernet *et al.* (2001) who used the dispersion of a wide laser beam that was reflected off the surface.

For measuring the wave amplitudes it was necessary to fix the spatial phase by pinning the surface in the square container at an excitation frequency (40 Hz) where a square pattern is preferred. Since the boundaries now matter, the results cannot strictly be compared to the infinite system case. The square container that we use has a width of 160 mm. The continuum would then start at $\varepsilon = 0.26$, which is already close to the disordered regime.

We will focus our attention on the behaviour of the linearly unstable waves and the waves which are generated by the nonlinear interactions between the linearly unstable waves. In terms of the theory, the linearly unstable waves correspond to the order $\varepsilon^{1/2}$, which we will call *subharmonic* waves, and the order ε term corresponds to the waves generated by the linearly unstable waves, which we will call *harmonic* waves. For a measurement of the phase we have devised methods that work for an unpinned pattern. These measurements, performed in the large container, should be free of boundary effects.

4.6.1. *The subharmonic wave*

The slowly varying amplitude $B_m(T)$ of the subharmonic wave satisfies the amplitude equation (2.3). For an N-fold rotational pattern the stationary amplitude is given by

$$B = \varepsilon^{1/2} (\gamma\omega)^{1/2} \left(g_0 + \sum_{m=2}^{N} g(\Theta_{m1}) \right)^{-1/2} . \tag{4.2}$$

In the weakly nonlinear case, therefore, the amplitude grows as $\varepsilon^{1/2}$ with the distance ε above threshold. An experimental test of this relation is highly relevant as it delineates the range of applicability of a weakly nonlinear approach.

In a square container, slow upward scans of ε were made. At each ε, a time series of the time-dependent slope was registered, from which the power spectrum was computed. Even in a square container, square patterns with a slightly different spatial phase may be selected when the excitation amplitude is increased from zero. To circumvent this, we repeat the experiment by decreasing ε slowly towards threshold, and just above threshold start increasing again, so that we keep the same spatial mode. This procedure is repeated ten times. For each value of ε, the power spectra of the measured slope are averaged. The area underneath the first peak in the power

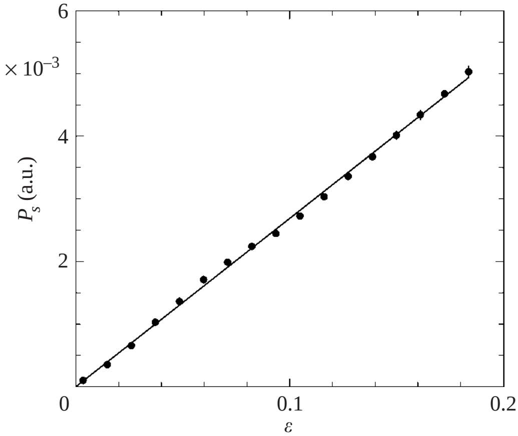

FIGURE 17. Scaling of the power P_s of the subharmonic wave with ε. Excitation frequency 40 Hz. The error bars (which are almost always obscured by the dots) denote the uncertainty of the measured power; the full line is a fit to the data which demonstrates that the wave amplitude grows as $\varepsilon^{1/2}$.

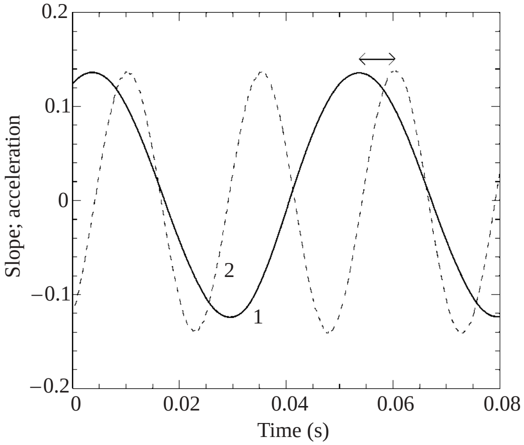

FIGURE 18. Relation between excitation and surface slope. —, measured surface slope as a function of time for $\varepsilon = 0.02$ and $F = 50$ Hz. – – –, measured acceleration of the container. The arrow denotes the phase difference between the two. In terms of the excitation, the wave lags by 90°. In terms of the subharmonic wave, the excitation heads by 45°.

spectrum is proportional to A^2, so the total power P_s in the area should scale as ε. The results of this procedure are shown in figure 17. It is clear that the bifurcation is supercritical, and the expected scaling holds up to at least $\varepsilon = 0.2$. After this value of ε, the pattern often develops defects, so the spatial phase is not constant anymore.

4.6.2. *The temporal phase of the subharmonic wave*

Another prediction of the weakly nonlinear theory that can be verified experimentally concerns the temporal phase of the harmonic waves as a function of the reduced excitation amplitude ε. This prediction was computed by us from the theory by Chen & Viñals (1999) using symbolic manipulation software that was kindly provided by them. The definition of the phase is shown in figure 18. It is seen that we define all phase differences in terms of the harmonic frequency.

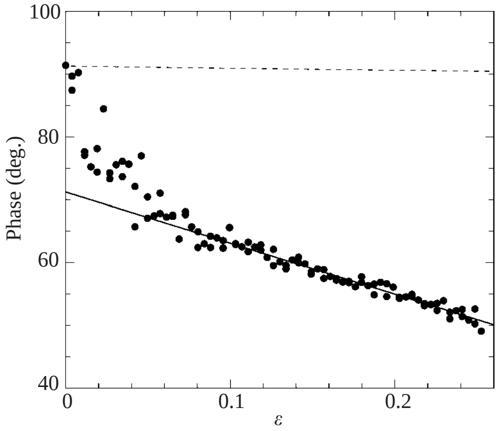

FIGURE 19. Phase of the subharmonic wave with respect to the excitation as a function of ε. The solid line is a linear fit through the data between $\varepsilon = 0.1$ and $\varepsilon = 0.25$. The dashed line is the theoretical phase from the linear stability analysis.

Since a measurement of the phase is in principle insensitive to the amplitude of the standing waves, it is no longer necessary to pin the surface. Therefore, these measurements were done in the large container with 0.44 m diameter. In order to cope with the drift of the surface wave pattern, we used the following procedure. The phase and the power of the subharmonic wave in a short stretch of data, containing an integer number of wave periods (4 . . . 8), is determined by means of a Fourier transform. The procedure is repeated with a different stretch of data, shifted by one wave period. In other words, a window with the size of an integer number of wave periods is slid over the data, and for each position the phase and power is computed. Notice that in our definition, the phase of a crest is the same as that of a trough, so that the phase does not depend on the spatial location where it is measured. Of course, a problem arises if this location happens to be at a node of the wave pattern. These problematic points were avoided by rejecting measurements that had too small a spectral power. The result is depicted in figure 19. The phase lag of the Mathieu equation is 90°; the linear theory of surface waves predicts a value (also shown in figure 19) that is slightly higher. At very small ε, the measured phase tends to this limit. For increasing ε, it first experiences a rapid decrease, after which it decreases more slowly, and apparently linearly with ε. We do not understand this behaviour. Perhaps, the first rapid decrease is a finite size effect, and the phase in the unbounded system is the one that can be linearly extrapolated to $\varepsilon = 0$ from the large-ε behaviour.

4.6.3. *The harmonic wave*

Through nonlinear interactions the subharmonic waves generate harmonic waves which have the same frequency as the excitation. As two subharmonic waves generate a harmonic wave, the amplitude of the latter scales as ε. We perform a scan in ε in the square container, in the same way as before. The power in the harmonic wave P_h, which is proportional to the amplitude squared, should scale as ε^2. The result is shown in figure 20. The expected scaling holds very well up to $\varepsilon = 0.2$, where the pattern starts to be distorted by defects.

The phase of the harmonic wave was obtained in the same way as the subharmonic wave. The phase of the harmonic wave with respect to the excitation as a function of

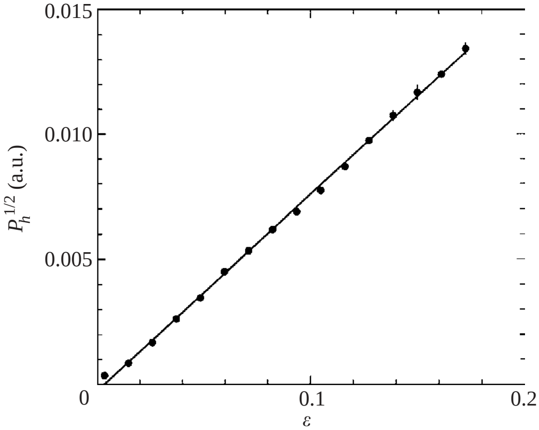

FIGURE 20. Scaling of the power P_h of the harmonic wave with ε. The solid line is a linear fit through the data. As there is a small uncertainty in the value of the onset, the fit was not forced to go through (0, 0).

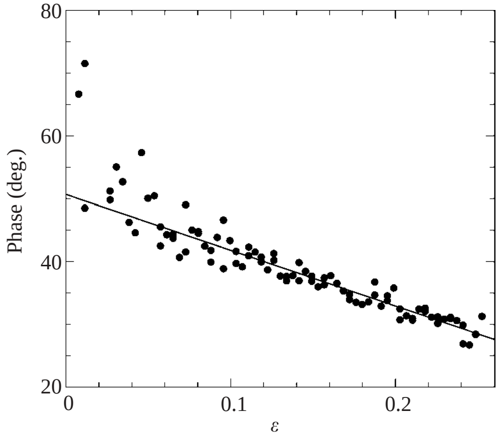

FIGURE 21. Phase of harmonic wave with respect to the excitation as a function of ε. The solid line is a linear fit through the data between $\varepsilon = 0.1$ and $\varepsilon = 0.25$.

ε is shown in figure 21. We see that the behaviour of the phase is exactly the same as for the subharmonic wave, the only difference is that it is shifted by a fixed amount, which is independent of ε. Therefore, the phase difference between the two waves is a well-defined quantity, independent of ε.

To simplify the computation of the phases, we only consider self-interaction between the waves. Because the self-interaction coefficient is much larger than the coupling of perpendicular waves, self-interaction dominates in the square pattern.

A subtle point is that what we compute is not exactly what we measure. The experimental subharmonic wave field is the sum of all terms in the theory that involve odd powers of $\varepsilon^{1/2}$, whereas the harmonic field consists of all terms involving even powers of $\varepsilon^{1/2}$. In the calculation, we only consider terms of order $\varepsilon^{1/2}$ and of order ε, for the subharmonic and harmonic waves, respectively. Still, we believe that the phase difference between these terms is the same as that between the harmonic and subharmonic waves.

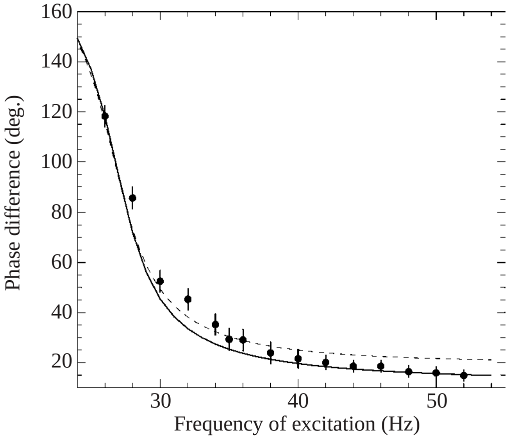

FIGURE 22. Phase difference between subharmonic and harmonic wave as a function of the excitation frequency. The phase difference is independent of ε. ●, experimental values; —, theoretical values according to Chen & Viñals (1999); – – –, theoretical values according to Zhang (1994).

In figure 22, we show the experimental values for the phase difference between the subharmonic and harmonic waves as a function of frequency. At each frequency, many runs were performed at different ε, and it was verified that the phase difference is independent of ε. The error bars represent the standard deviation in the observed values for the phase.

The experiments are in striking agreement with theory; we even notice that the theory by Chen & Viñals (1999), which is an improvement over that by Zhang (1994), agrees best with the experiment. The agreement is poorest around the frequency of the three-wave resonance (28 . . . 38 Hz) where the non-self wave interactions which were ignored in our computation become important.

4.6.4. *Spatial structure of the wave field*

The weakly nonlinear wave field has, in fact, a very complicated structure. Several waves of various frequencies collaborate to provide the nonlinear dissipation that determines the amplitude of the wave field. It is interesting to see how these waves are organized in space. This can only be done in an experiment with an extremely linear detector of wave heights or wave slopes. Shadowgraph techniques are completely unsuitable for studying the fine details of the standing-wave pattern.

For these experiments we pinned a square standing-wave pattern at an excitation frequency $F = 64$ Hz and a reduced excitation amplitude $\varepsilon = 0.15$ in a square container. We then sampled time series of point measurements of the slope in 62 points, on a line of length 15.5 mm. At each of these points, we computed the power spectrum of the signal. The wave amplitude at frequencies ω_0 (subharmonic), $2\omega_0$ (harmonic) and $3\omega_0$ is shown in figure 23. A first striking observation is that the nodes of the subharmonic waves are also nodes of the harmonic wave, which has half the wavelength of the subharmonic wave. This can be understood from the dominance of the self-interaction in this square wave pattern. It is also remarkable, but not surprising, that the harmonic wave does not satisfy the dispersion relation.

Surprisingly, also the wave at $3\omega_0$ can be clearly seen. It has wavelength equal to three times the wavelength of the subharmonic. It is generated by an interaction of the subharmonic with the harmonic. The variation in amplitude of the maxima

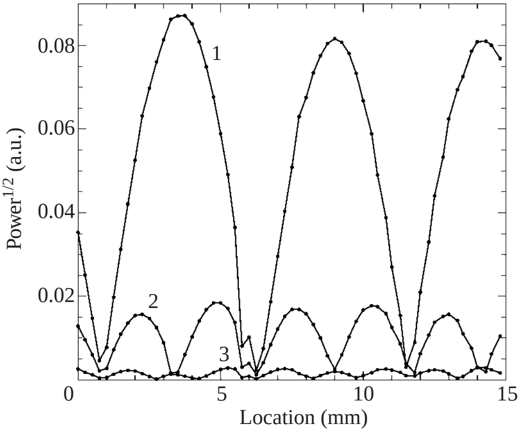

FIGURE 23. Scan over a square pattern, with $F = 64$ Hz and $\varepsilon = 0.15$. The scan direction was parallel to one of the waves constituting the pattern. The amplitude (derived from the power spectrum of the slope) of the subharmonic 1, harmonic 2, and the wave at $3\,\omega_0$, 3, are shown as a function of position. As we measure the power, we can only retrieve the absolute value of the amplitude. The irregularity around 6 mm is probably due to a scratch in the glass.

is probably caused by a misalignment of the scanning direction with respect to the pattern.

5. Conclusion

In this paper we have presented measurements that check the linear instability theory and the weakly nonlinear theory of pattern formation introduced in § 2 The threshold of the instability and the dispersion relation for finite depth were shown to agree with the theoretical estimates. Indeed, the linear stability theory for Faraday waves is so well developed that we expect that Faraday waves may be used as an alternative technique to measure fluid parameters such as viscosity and surface tension with great precision.

The phase diagram for pattern formation was shown to agree precisely with the theory by Chen & Viñals (1999). In the case of finite depth, we have shown that the change in the pattern formation can be understood from the change in the shape of the dispersion relation with depth. Together with the toy model we have introduced, this provides a convincing proof that pattern formation of Faraday waves can be understood as a three-wave resonance phenomenon.

By using an extremely linear measurement technique, we have been able to directly test quantitative predictions on the wave field. The scaling and the phase of both the harmonic and the subharmonic waves were shown to give excellent agreement with theoretical estimates. Finally, a surface scan was presented which clearly shows the nonlinearly generated waves and their positions for the first time.

This paper also describes a concentrated effort to study nonlinear hydrodynamics in systems that are so large that the boundaries are no longer relevant. Thus, we are focusing on an intrinsic property of the nonlinear wave field. We believe that this is a more interesting problem than a study of the influence of boundaries. Boundaries can be made of any form and shape, each introducing its own peculiarity. Another way to make a system effectively large is to use a fluid with high viscosity (Edwards & Fauve 1994), as this decreases the correlation length of the system. However, in this case we would have missed the cascade of patterns of increasing rotational symmetry near the point of three-wave resonance.

In view of the very favourable agreement between experiment and theory we may conclude that the problem of weakly nonlinear Faraday waves and the surface patterns they form is a solved problem. However, the amplitudes of the standing waves considered here do not have a space dependence: the patterns arise by combining N of them with equal amplitudes distributed at equal angles on the circle. Other than a local phase ambiguity in §4.4, we have not considered an essential spatial dependence. A spatial structure of the slow amplitude field $B(\boldsymbol{x}, T)$ can be described by extending (1.1) with a diffusion term and allowing B to be complex. The resulting equation, the complex Ginzburg–Landau equation, has proved to be a powerful organizing principle to understand pattern formation and the emergence of coherent structures, such as defects and fronts (Cross & Hohenberg 1993). Unfortunately, weakly nonlinear Faraday waves have a large correlation length ξ and extremely large experiments would be required to study spatial effects of three-wave coupling.

Further above onset ($\varepsilon > 1$), the surface becomes turbulent and develops a continuous energy spectrum. As the main energy transfer is still through three-wave interaction and because the dissipation is small, the turbulent state is thought to be a manifestation of weak turbulence (Zakharov, L'vov & Fal'kovich 1992). It is also here that a big experiment may help to overcome finite-size effects.

We are indebted to Wim van Saarloos who pointed out the importance of the correlation length ξ in an early stage of this project. We also thank Gerald Oerlemans for technical assistance. Financial support by the 'Nederlandse Organisatie voor Wetenschappelijk Onderzoek (NWO)' and by 'Stichting Fundamenteel Onderzoek der Materie (FOM)' is gratefully acknowledged.

REFERENCES

Bechhoefer, J., Ego, V., Manneville, S. & Johnson, B. 1995 An experimental study of the onset of parametrically pumped surface waves in viscous fluids. *J. Fluid Mech.* **288**, 351–381.

Benjamin, T. & Ursell, F. 1954 The stability of the plane surface of a liquid in vertical periodic motion. *Proc. R. Soc. Lond.* A **225**, 505–515.

Binks, D. & van de Water, W. 1997 Nonlinear pattern formation of Faraday waves. *Phys. Rev. Lett.* **78**, 4043–4046.

Bosch, E., Lambermont, H. & van de Water, W. 1994 Average patterns in Faraday waves. *Phys. Rev.* E **49**, R3580–R3583.

Bosch, E. & van de Water, W. 1993 Spatiotemporal intermittency in the Faraday experiment. *Phys. Rev. Lett.* **70**, 3420–3423.

Chen, P. & Viñals, J. 1999 Amplitude equations and pattern selection in Faraday waves. *Phys. Rev.* E **60**, 559–570.

Christiansen, B., Alstrøm, P. & Levinsen, M. 1992 Ordered capillary-wave states: quasicrystals, hexagons, and radial waves. *Phys. Rev. Lett.* **68**, 2157–2160.

Ciliberto, S., Douady, S. & Fauve, S. 1991 Investigating space–time chaos in Faraday instability by means of the fluctuations of the driving acceleration. *Europhys. Lett.* **15**, 23–28.

Ciliberto, S. & Gollub, J. 1985 Chaotic mode competition in parametrically forced surface waves. *J. Fluid Mech.* **158**, 381–398.

Crawford, J. 1991 Surface waves in nonsquare containers with square symmetry. *Phys. Rev. Lett.* **67**, 441–444.

Crawford, J. 1993 Hidden symmetries of parametrically forced waves. *Nonlinearity* **6**, 119–164.

Cross, M. & Hohenberg, P. 1993 Pattern formation out of equilibrium. *Rev. Mod. Phys.* **65**, 851–1112.

DAUDET, L., EGO, V., MANNEVILLE, S. & BECHHOEVER, J. 1995 Secondary instabilities of surface waves on viscous fluids in the Faraday instability. *Europhys. Lett.* **32**, 313–318.

EDWARDS, W. & FAUVE, S. 1994 Patterns and quasi-patterns in the Faraday experiment. *J. Fluid Mech.* **278**, 123–148.

EGUÍLUZ, V., ALSTRØM, P., HERNÁNDEZ-GARCÍA, E. & PIRO, O. 1999 Average patterns of spatiotemporal chaos: a boundary effect. *Phys. Rev.* E **59**, 2822–2825.

EZERSKII, A. 1991 Temporal intermittency of chaos in parametrically excited capillary ripples. *Europhys. Lett.* **16**, 661–666.

EZERSKII, A., KIYASHKO, S., MATUSOV, P. & RABINOVICH, M. 1994 Domains, domain walls and dislocations in capillary ripples. *Europhys. Lett.* **26**, 183–188.

EZERSKII, A. & RABINOVICH, M. 1990 Nonlinear wave competition and anisotropic spectra of spatio-temporal chaos of Faraday ripples. *Europhys. Lett.* **13**, 243–249.

EZERSKII, A., RABINOVICH, M., REUTOV, V. & STAROBINETS, I. 1986 Spatiotemporal chaos in the parametric excitation of a capillary ripple. *Zh. Éksp. Teor. Fiz.* **91**, 2070–2083 (English trans. Sov. Phys., *J. Exp. Theor. Phys.* **64**, 1228–1236, 1986).

FAUVE, S., KUMAR, K., LAROCHE, C., BEYSENS, D. & GARRABOS, Y. 1992 Parametric instability of a liquid–vapour interface close to the critical point. *Phys. Rev. Lett.* **68**, 3160–3163.

FENG, Z. & SETHNA, P. 1989 Symmetry-breaking bifurcations in resonant surface waves. *J. Fluid Mech.* **199**, 495–518.

GLUCKMAN, B., ARNOLD, C. & GOLLUB, J. 1995 Statistical studies of chaotic wave patterns. *Phys. Rev.* E **51**, 1128–1147.

GLUCKMAN, B., MARCQ, P., BRIDGER, J. & GOLLUB, J. 1993 Time averaging of chaotic spatiotemporal wave patterns. *Phys. Rev. Lett.* **71**, 2034–2037.

GOLLUB, J. 1991 Nonlinear waves: dynamics and transport. *Physica* D **51**, 501–511.

GOLLUB, J. & MEYER, C. 1983 Symmetry-breaking instabilities on a fluid surface. *Physica* D **6D**, 337–346.

GOLLUB, J. & RAMSHANKAR, R. 1991 In *New perspectives in Turbulence* (ed. L. Sirovich). Springer.

HENDERSON, D. & MILES, J. 1994 Surface-wave damping in a circular cylinder with a fixed contact line. *J. Fluid Mech.* **275**, 285–299.

KUDROLLI, A. & GOLLUB, J. 1996 Patterns and spatiotemporal chaos in parametrically forced surface waves: a systemetic survey at large aspect ratio. *Physica* D **97**, 133–154.

KUMAR, K. 1996 Linear theory of Faraday instability in viscous liquids. *Proc. R. Soc. Lond.* A **452**, 1113–1126.

KUMAR, K. & BAJAJ, K. 1995 Competing patterns in the Faraday experiment. *Phys. Rev.* E **52**, R4606–R4609.

KUMAR, K. & TUCKERMAN, L. 1994 Parametric instability of the interface between two fluids. *J. Fluid Mech.* **279**, 49–68.

LANG, R. 1962 *J. Acoust. Soc. Am.* **34**, 6.

LIOUBASHEVSKI, O., FINEBERG, J. & TUCKERMAN, L. 1997 Scaling of the transition to parametrically driven surface waves in highly dissipative systems. *Phys. Rev.* E **55**, R3832–R3835.

MATTHIESSEN, L. 1868 *Annln Phys., Lpz.* **134**, 107.

MATTHIESSEN, L. 1870 *Annln Phys., Lpz.* **141**, 375.

MERON, E. & PROCACCIA, I. 1986*a* Low-dimensional chaos in surface waves: theoretical analysis of an experiment. *Phys. Rev.* A **34**, 3221–3237.

MERON, E. & PROCACCIA, I. 1986*b* Theory of chaos in surface waves: the reduction from hydrodynamics to few-dimensional dynamics. *Phys. Rev. Lett.* **56**, 1323–1326.

MILES, J. 1984 Nonlinear Faraday resonance. *J. Fluid Mech.* **146**, 285–302.

MILES, J. 1993 On Faraday waves. *J. Fluid Mech.* **248**, 671–683.

MILES, J. & HENDERSON, D. 1990 Parametrically forced surface waves. *Annu. Rev. Fluid Mech.* **22**, 143–165.

MILES, J. & HENDERSON, D. 1998 A note on interior vs. boundary-layer damping of surface waves in a circular cylinder. *J. Fluid Mech.* **364**, 319–323.

MILNER, S. 1991 Square patterns and secondary instabilities in driven capillary waves. *J. Fluid Mech.* **225**, 81–100.

MÜLLER, H. 1993 Periodic triangular patterns in the Faraday experiment. *Phys. Rev. Lett.* **71**, 3287–3290.

Müller, H., Wittmer, H., Wagner, C., Albers, J. & Knorr, K. 1997 Analytic stability theory for Faraday waves and the observation of the harmonic surface response. *Phys. Rev. Lett.* **78**, 2357–2360.

Ning, L., Hu, Y., Ecke, R. & Ahlers, G. 1993 Spatial and temporal averages in chaotic patterns. *Phys. Rev. Lett.* **71**, 2216–2219.

Rayleigh, Lord 1883*a* On maintained vibrations. *Phil. Mag.* **15**, 229–235.

Rayleigh, Lord 1883*b* On the crispations of a fluid resting upon a vibrating support. *Phil. Mag.* **16**, 50–58.

Simonelli, F. & Gollub, J. 1989 Surface wave mode interactions: effects of symmetry and degeneracy. *J. Fluid Mech.* **199**, 471–494.

Tufillaro, N., Ramshankar, R. & Gollub, J. 1989 Order–disorder transition in capillary ripples. *Phys. Rev. Lett.* **62**, 422–425.

Umeki, M. 1991 Faraday resonance in rectangular geometry. *J. Fluid Mech.* **227**, 161–192.

Wernet, A., Wagner, C., Papathanassiou, D., Müller, H. & Knorr, K. 2001 Amplitude measurements of Faraday waves. *Phys. Rev.* E **63**, 36 305–36 309.

Wright, W., Budakian, R. & Putterman, S. 1996 Diffusing light photography of fully developed isotropic ripple turbulence. *Phys. Rev. Lett.* **76**, 4528–4531.

Zakharov, V., L'vov, V. & Fal'kovich, G. 1992 *Kolmogorov Spectra of Turbulence*, 1st edn. Springer, Berlin.

Zhang, W. 1994 Pattern formation in weakly damped parametric surface waves. PhD thesis, Florida State University.

Zhang, W. & Viñals, J. 1996 Square patterns and quasipatterns in weakly damped Faraday waves. *Phys. Rev.* E **53**, R4283–R4286.

Zhang, W. & Viñals, J. 1997*a* Pattern formation in weakly damped parametric surface waves. *J. Fluid Mech.* **336**, 301–330.

Zhang, W. & Viñals, J. 1997*b* Pattern formation in weakly damped parametric surface waves driven by two frequency components. *J. Fluid Mech.* **341**, 225–244.

Zhang, W. & Viñals, J. 1998 Numerical study of pattern formation in weakly damped parametric surface waves. *Physica* D **116**, 225–243.